Final Report

NASA GSFC STTR Contract No. NAS5-96042

An Optical Extinctiometer for Cloud Radiation Measurements

February 2000

1.1 Introduction

The potential impact of **clouds** on global climate change was assessed as the highest scientific priority item by the U.S. Committee on Earth and Environmental Sciences (Source: *Our Changing Planet: The FY 1993 U.S. Global Change Research Program p. 6*). The principle influence clouds have on global warming is through their spatial extent and their radiative characteristics. A fundamental parameter used in equations of radiative transfer is the mass extinction coefficient (Liou 1980). In water clouds, the mass extinction coefficient is computed from the volumetric extinction coefficient, β_λ, assuming spherical drops composed of pure water. Numerical computations of radiative transfer and predictions of global climate change depend on accurate measurements of β_λ. The cloud extinctiometer, developed under this STTR research, is the first multi-wavelength, airborne instrument capable of making direct *in situ* measurements of β_λ in clouds. In Phase I, we designed a prototype cloud extinctiometer and tested it in the laboratory and on a mountaintop. In Phase II, we built and tested an airborne instrument on a research aircraft.

1.2 Background

Our understanding of the radiative impact of clouds on the environment is an evolving science. Data from Nimbus 7 and other earth radiation budget (ERB) satellites launched in the 1960s showed that clouds played a significant role in influencing the planetary albedo (e.g., House 1965; Von der Haar and Suomi 1969, 1971). Significant amongst the early findings was that the albedo of the two hemispheres is nearly the same, implying that clouds play a role which dominates surface effects, since the surface features are measurably different in the northern and southern hemispheres. Basically, clouds exert two major influences on the ERB:

i. Cloud albedo dominates the incoming short-wave solar insolation, and

ii. outgoing long-wave radiation is strongly affected by cloud absorption.

Liou (1980) shows that the principal equation used in radiative transfer is

$$dI_\lambda = \left(J_\lambda - I_\lambda\right)k_\lambda\, p\, ds \qquad (1)$$

where λ is wavelength, I_λ is the intensity of a pencil beam of radiation, J_λ is the intensity of emission from material within the beam and multiple scattering into the beam from all other directions, k_λ is the mass extinction coefficient, ρ is the density of the material and *ds* is thickness. In water clouds, the droplets (with diameters $<\sim 200\mu m$) are assumed to be spherical and composed of pure water so that k_λ can be replaced with β_λ.

The volumetric extinction coefficient is the sum of the scattering $\left(\beta_{s\lambda}\right)$ and absorption $\left(\beta_{a\lambda}\right)$ coefficients,

$$\beta_\lambda = \beta_{s\lambda} + \beta_{a\lambda}. \qquad (2)$$

Mie scattering theory gives an exact solution to Maxwell's equations for single-particle scattering. Using (2) and the assumption that water clouds contain spherical particles composed of pure water, Mie theory predicts the percentages of scattered and absorbed radiation.

There is general agreement that the annual global mean effect of clouds is to cool the climate system, however, satellite data suggest that the magnitude of this effect is uncertain, ranging from 17 to 27 W m^{-2} in two studies (see Arking 1991). Analyses of Nimbus 7 data by Ardanuy and Kyle (1986) have revealed long-wave flux anomalies exceeding ±50 mW in the equatorial Pacific during an El Niño event. Recently, Pilewskie and Valero (1995) showed convincing evidence that clouds absorb more solar radiation than previously believed (see Stephens and Tsay 1990 for a discussion of anomalous absorption). Using identical precision radiometers (Valero et al. 1983) mounted on two research aircraft, one above and one below cloud decks, Pilewskie and Valero (1995) found that the measured cloud absorption consistently exceeds theoretical estimates.

The effects described above (i.e., the influence clouds have on solar albedo, absorption of long-wave radiation and possible anomalous absorption of solar light) clearly dramatize the leverage clouds have on radiative aspects of the global climate system.

In this report, we present the work completed for the Phase II. We discuss the numerical modeling, design, assembly and testing of the airborne extinctiometer used to measure extinction coefficient in clouds. Results are presented for measurements taken by the airborne extinctiometer for three research flights.

1.3   Summary of Phase I Research.

In Phase I, data sets collected in the Former Soviet Union in the 1970s and 1980s with the "Russian Transmissometer" (Nevzorov and Shugaev 1974, Korolev et al 1999) were analyzed. The Russian transmissometer is an open path instrument using a modulated light emitting diode (LED) as a source that is pointed at a retroreflector mounted at a separate location on the aircraft. The detector is mounted adjacent to the source and synchronously detects the light beam bouncing off the retroreflector. Measurements of extinction coefficient were made using the transmissometer in a variety of conditions. Analysis of these measurements was used to determine a design range for the airborne cloud extinctiometer and to demonstrate the feasibility of comparing measurements made with the transmissometer to the cloud extinctiometer.

A prototype ground based cloud extinctiometer, operating over a single spectral waveband, was built and tested at Storm Peak Observatory. The observatory is located on top of Storm Peak at the Steamboat Springs ski area in Colorado and is operated by Desert Research Institute (DRI). **Figure 1** is a schematic of the optical system used in the ground based prototype. **Figure 2** is a photograph of the Phase I instrument installed at the Storm Peak observatory. **Figure 3** is a plot of the extinction coefficient measured by the ground based instrument at Storm Peak. The ground based measurements were adequate to demonstrate feasibility of an airborne cloud extinctiometer based on this measurement technique.
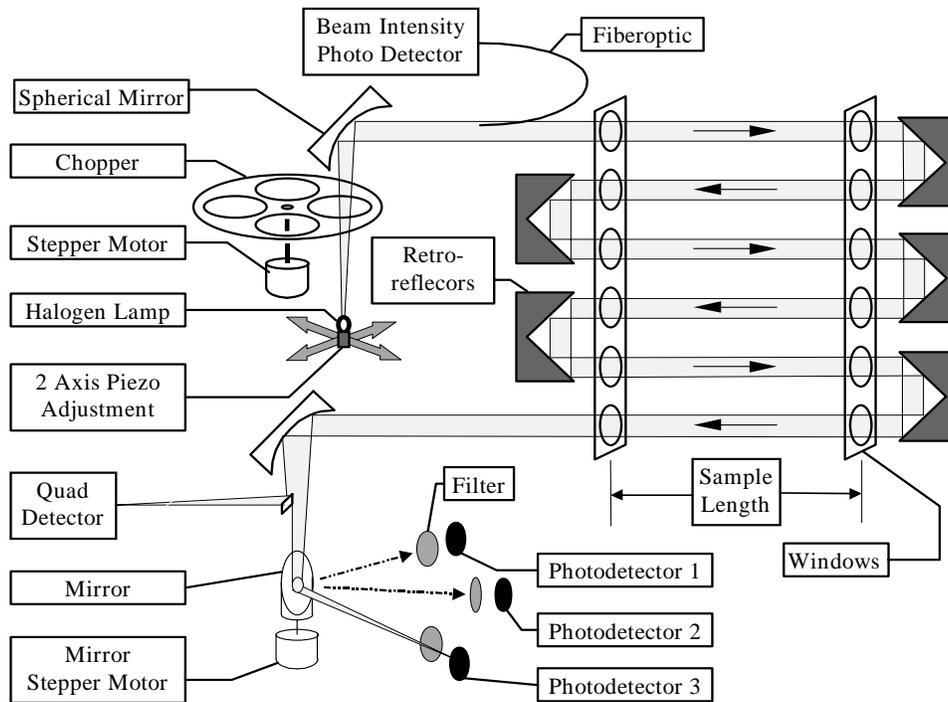

Figure 1. Schematic of Phase I design. Only 1 photodetector is used for the Phase I instrument.

1.4 Summary of Work Performed in of Phase II

1.4.1 Phase II Technical Objectives

The proposed technical objectives for the Phase II research were:

1. Fabricate a prototype airborne single-wavelength cloud extinctiometer and test it along with the Russian transmissometer and SPEC ACS at the Storm Peak Observatory and analyze the results.
2. Modify the cloud extinctiometer to include three wave bands of measurement.
3. Flight test the modified cloud extinctiometer, Russian Transmissometer and SPEC ACS on a Cessna 337 in water clouds and analyze the results.

Figure 2. The SPEC automatic cloud spectrometer (ACS)(left) and the cloud extinctiometer (right) mounted on a rail on the roof of Storm Peak Observatory.
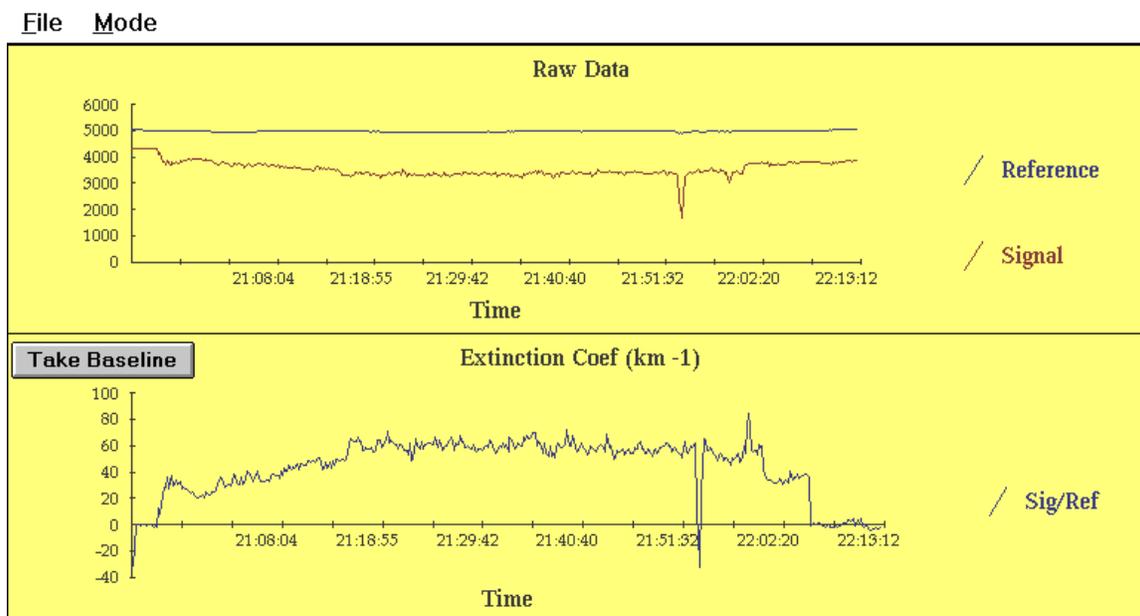

Figure 3. A screen print from the real-time display of parameters from the cloud extinctiometer. The portions where extinction coefficient is near zero at the beginning and end of the time series are the result of "cloaking" to measure baseline. The negative spike is when a technician put his hand in the sample volume.

4. Flight test the modified cloud extinctiometer, Russian Transmissometer and SPEC ACS on a Learjet in cirrus and analyze the results.

5. Perform proof-of-concept experiments to determine the extinctiometer can be modified to make measurements in dust-laden environments and of water turbidity.

1.4.2 Work Performed in Phase II

The overall technical objectives of designing, fabricating, and flying an airborne cloud extinctiometer were accomplished. As the instrument development progressed, the specific objectives listed above were modified to better meet the overall technical objective of developing a reliable instrument. At the request of the technical contracting officer, numerical modeling of the instrument was performed to aid in the instrument design and to better interpret the data collected with the airborne cloud extinctiometer.

The initial design proposed in Phase I was altered based on technical information that became available after the Phase I work was completed. The multiple retroreflector system was replaced with a Herriott cell based system to provide a simpler, more reliable design. To verify this design, ground based tests were not performed at Storm Peak, but in an all water cloud chamber built at SPEC. The Russian transmissometer and a Forward Scattering Spectrometer (FSSP) (Knollenberg 1981) were installed in the chamber for comparison. The FSSP was used instead of the SPEC ACS because the ACS was not available during the period of this research and the measurements of drop size and concentration made using the FSSP are easily used to calculate extinction. The testing occurred very early in the design stage to provide a solid technical foundation for the work that followed. More ground based testing was completed in a wet wind tunnel, to simulate flight conditions and to evaluate the robustness of the optical system to operate in a contamination prone environment. Testing in an environmental chamber was performed to evaluate the effect of temperature changes encountered in the atmosphere on the measurements made with the instrument.

The completed instrument, operating at three spectral channels, was test flown on the SPEC Learjet. A suite of other research instrumentation, including the Russian Transmissometer, SPEC Cloud Particle Imager (CPI), a Particle Measuring Systems (PMS) Forward Scattering Spectrometer (FSSP) and a PMS 2D-C probe (Knollenberg 1981) were also mounted on the aircraft and available for comparisons to the extinctiometer. A total of four research flights were made with the airborne cloud extinctiometer.

2.0 Design of Phase II Instrument

2.1 Overview

The extinction process can be described by Beer's Law,

$$\frac{I}{I_o} = exp(-\beta_\lambda X)$$ (3)

where I_o is the incident light intensity, I is the transmitted intensity, X is the path length, and β_λ is the volumetric extinction coefficient. In principle, the cloud extinctiometer is a fairly simple instrument consisting of a light source which produces a beam of light that falls on a detector. In this case, I_o is the light intensity falling on the detector with no cloud particles in the beam and I is the light intensity falling on the detector with particles attenuating the beam. The path length is a system constant. Extinction is the sum of the scattered and absorbed radiation when cloud particles (spherical drops or ice crystals) interact with the light beam. The volumetric extinction coefficient is calculated from the ratio of the attenuated beam intensity to the incident beam intensity.

2.1.1 Determination of Optical Path Length

The optical path length for the system was determined by optimizing the instrument for the minimum and maximum values of extinction to be measured. **Figure 4a** is a plot of β_λ versus I/I_o as a function of path length. Based on analysis of the Russian Transmissometer data set analyzed in Phase I, the instrument should be capable of measuring extinction coefficients ranging from 1 to 200 km^{-1}. **Figure 4a** shows that for a path length of 25 m, sensitivity is decreased for values of β_λ>100 because the transmitted to incident light ratio begins to saturate. A path length of 5 m results in approximately 60% of the light being attenuated for β_λ=200. For a range of 1<β_λ<200 km^{-1}, path lengths of 10 and 15 m appear to give the best sensitivity throughout the range.
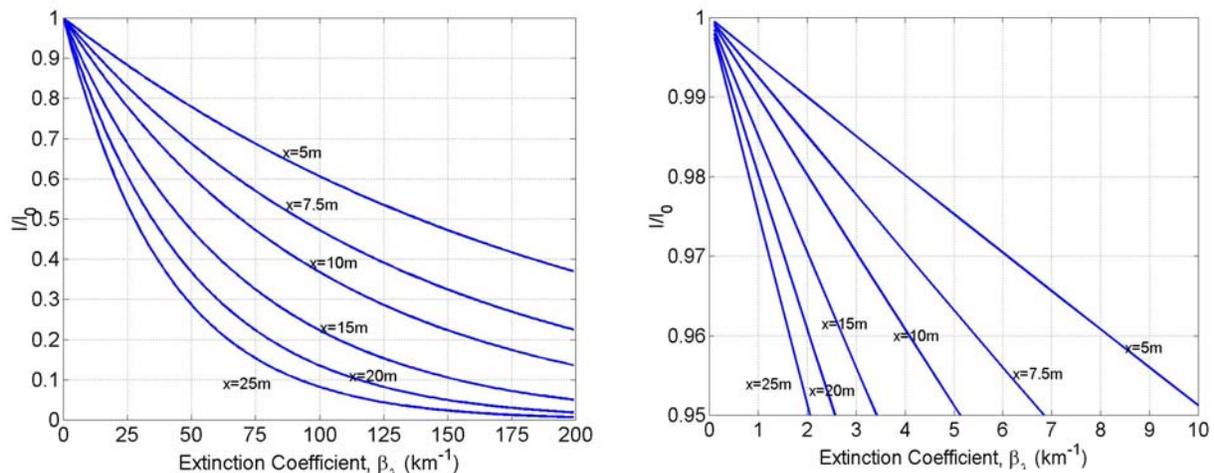

Figure 4. a) (left) Extinction coefficient versus attenuation of incident light as a function of path length. **b)** (right) lower extinction region of previous plot.

The lowest value to be measured is β_λ =1 km^{-1} or less. The lower detectable limit for the measurement will depend on having an adequate signal to noise ratio (SNR). The Phase I instrument had a target noise floor of 0.1% and the actual noise was a factor of five better than 0.1% in the laboratory. Using the more conservative estimate for noise of 0.1%, **Figure 4b** shows that for β_λ=1, a path length of 5 m will attenuate about 0.5% of the incident light and have a SNR= 5:1. A 10 m path length will attenuate 1% of the incident light an yield a SNR=10:1.

2.1.2 Herriott Cell versus Retroreflector Design

The ground based instrument built in Phase I used a retroreflector based system to achieve an optical path length of approximately 3 m. A similar type of retroreflector configuration was also proposed to achieve the long path length necessary for the airborne instrument. An airborne instrument will experience vibrations and temperature changes much greater than those found in a ground-based environment. Based on the sensitivity of the Phase I instrument to mild vibrations and small temperature changes, an airborne instrument utilizing this type of design would require an active control system to maintain the optical alignment. One technique for doing this is to use piezo-electric actuators to steer the retroreflectors to maintain a constant baseline signal. This approach would result in a cumbersome and overcomplicated design. An alternative design utilizing a multipass Herriott cell (Herriott et al 1964) was used for the airborne extinctiometer to alleviate the need for an active alignment system.

Herriott Cell Description

A Herriott cell is a multipass optical cavity that consists of two concave spherical mirrors separated by a fixed distance. The inlet beam is injected into the cell at an angle ϕ through a hole in one of the mirrors. If the re-entrant condition is met, the beam exits at an angle different than ϕ through the same hole after multiple passes through the cell. **Figure 5** is a schematic drawing of a Herriott cell. For the general case, the beam bounces back and forth between the mirrors tracing an elliptical spot pattern on each mirror. For a particular set of injection angles, the spot pattern will be circular on each mirror, thereby using the mirror aperture most efficiently.

The following equations (Trutna and Byer 1980) can be used to describe the behavior of the cell. The resonator parameter, g, is defined by:

$$g=1-L/R \qquad (4)$$

where L is the separation between the two mirrors, and R is the radius of curvature for the concave spherical mirrors.

$$\theta=\cos^{-1}(2g^2-1) \qquad (5)$$

is the angle between successive reflected spots.

The re-entrant condition is stated as

$$2\pi K = n\ \theta \qquad\qquad (6)$$

where n and K are integers. After n round trips through the cell the beam returns to the entrance location (Herriott et al. 1964).

The alignment stability for this type of resonator is inherently more stable than the retroreflector system proposed in Phase I. The cell is relatively insensitive to slight angular and rotational misalignments of the mirrors: i.e., the reentrant condition will still be maintained. A Herriott cell is also much more spatially efficient, achieving a much greater pathlength in a smaller volume than a retroreflector based system. This type of cell has been used extensively to make long path absorption measurements in a variety of environments (Webster et al. 1994, May 1998). Using a Herriott cell to achieve the long pathlength necessary for the airborne extinctiometer results in a more robust design and a smaller overall package for the instrument.

2.1.3 Specification of Spectral Wavebands

The design proposed in Phase I called for three wavebands to be detected. The bands were 0.4 – 1.1 µm, 1.1 –1.7 µm and 1.7 –2.4 µm. After further discussions with members of the remote sensing and climate modeling communities, the requirements for the specific wavebands were changed to wavelengths of more scientific interest. The above mentioned bands are much too wide due to the variance in the intensity of the solar spectrum over this range and due to large changes in molecular absorption. The desired solution would be to have a spectrometer that looked at a very high number of narrow bands. As a compromise,100 nm wide bands were suggested, three to twelve bands total.

In the visible region, the bands selected are from 0.4 -0.5 µm, 0.5-0.6 µm and 0.6-0.7 µm. These particular bands are of interest because they contain some unknown molecular absorptions. The 0.4 – 0.5 µm range in particular has a recently discovered unknown molecular absorption.

At longer wavelengths, bands centered around 1.64 µm and 2.2 µm were chosen based on the interest of these bands in the remote sensing community. The Moderate Resolution Imaging Spectrometer (MODIS), part of the experimental payload on the Terra (EOS AM-1, launched December 1999) and Aqua (EOS PM-1, scheduled launch December 2000) satellites, uses these "windows" to look through the atmosphere to the ground because of the low molecular absorption in these regions. Extinction in these bands should be primarily due to cloud drops.

A waveband centered around 1.37 µm would be of interest due to the very high molecular absorption in this region. There is a relatively new MODIS channel at this wavelength. A channel exists at 0.94 µm with high molecular

absorption, but this region has been relatively well studied, so there is more new information to be gained in the 1.37 µm region. These regions are used by MODIS for looking at cirrus clouds without any ground noise, since this wavelength is attenuated in the lower atmosphere. **Table I** shows the selected wavelengths corresponding to each spectral channel for the extinctiometer.

Detector	Channel Number	Center Wavelength (± Tolerance)	Bandwidth (FWHM) (± Tolerance)	Notes
Detector #1 Silicon	Channel 1	450 nm (± 14 nm)	70 nm (± 14 nm)	-
	Channel 2	550 nm (± 14 nm)	70 nm (± 14 nm)	-
	Channel 3	650 nm (± 14 nm)	70 nm (± 14 nm)	-
	Channel 4	750 nm (± 14 nm)	70 nm (± 14 nm)	-
	Channel 5	850 nm (± 14 nm)	70 nm (± 14 nm)	-
	Channel 6	950 nm (± 14 nm)	70 nm (± 14 nm)	-
Detector #2 1.9µm Extended InGaAs	Channel 7	$1.375\mu m$(± 6 nm)	30 nm (± 6 nm)	MODIS Channel 26 used for Cirrus Clouds and Water Vapor
	Channel 8	$1.640\mu m$(± 5 nm)	25 nm (± 5 nm)	MODIS Channel 6 used for Cloud Properties
Detector #3 2.6µm Extended InGaAs	Channel 9	$2.130\mu m$(± 10 nm)	50 nm (± 10 nm)	MODIS Channel 7 used for Cloud Properties

Table I. Center wavelengths and bandwidths for each of the extinctiometer channels.

2.2 Numerical Modeling

Numerical modeling was performed to aid in design and to assist in the interpretation of the data collected with the cloud extinctiometer. A perfect measurement of extinction would not measure any of the light scattered by a particle, but only the attenuation of the incident beam caused by the particle passing through the beam. However, since most measurements of extinction utilize a detector located along the axis of the incident beam, some of the forward-scattered light from a particle intersecting the beam reaches the detector. This can be thought of as a "contamination" of the measured value of extinction. The problem is further compounded in a Herriott cell because the light which is forward-scattered by a particle is refocused each time it intercepts one of the spherical mirrors.

The analysis can be broken into two parts. In order to understand how the extinction measurement is affected by forward-scattered light propagating through the Herriott cell, it is first necessary to understand how the Herriott cell geometry influences light scattered at various angles within the cell. This part of the problem can be solved using ray tracing techniques.

The next part of the problem requires calculating the theoretical value of extinction for various water drop sizes and wavelengths and combining it with the

angular scattering dependence of the Herriott cell. Mie theory predicts the angular distribution and intensity of a plane electromagnetic wave scattered by a dielectric sphere. For a pure water drop in air, the amount of light scattered into the forward diffraction peak is dependent on the Mie size parameter, which is a function of wavelength and drop size. For a given wavelength, large particles scatter more light into the forward diffraction peak than small particles. The calculated scattering phase functions must be combined with the refocusing effect of the Herriott cell to predict how extinction measured using a Herriott cell compares to calculated extinction.

2.2.1   Effect of Herriott Cell on Angular Scattering

Based on the results in **Section 2.1.1**, describing the required optical pathlength for the airborne cloud extinctiometer, angular scattering calculations were performed for three Herriott cell geometries. **Table 2** lists the parameters for the three cells investigated. The first geometry modeled is a 30 pass cell with a mirror spacing 0.302 m, a mirror radius of curvature of 0.914 m and a total path length of 9.06 m. The second geometry modeled is for a 26 pass cell with a mirror spacing of .319 m, a radius of curvature of 1.27 m and a total path length of 8.29 m. The third Herriott cell has 18 passes, a spacing of 0.296 m, a mirror curvature of 1.27 m and a total path of 5.27 m. Detailed results are presented for the 30 pass cell in the next section. The final output functions for the three Herriott cells are then compared.

Total passes N	Round trip passes n=N/2	Mirror Separation L (m)	Mirror Radius of Curvature R (m)	Resonator Parameter g	Angle Between spots Θ (rads)	Reentrant parameter K	Path length X (m)
30	15	0.3025	0.9144	0.66913	1.6755	4	9.06
26	13	0.3194	1.27	0.74851	1.4499	3	8.29
18	9	0.2966	1.27	0.766045	1.3963	2	5.27

Table 2. Comparison of Herriott cell parameters for the three configurations investigated.

2.2.1.1   Dependence of Scattered Light Collected on Position along Beam Path

The first part of the modeling involves calculating the fraction of scattered light reaching the exit aperture as a function of position along the beam. **Figure 6** is a ray trace of the Herriott cell generated using Zeemax™ optical design software. The configuration of the cell is the same as the one prototyped in the laboratory cloud chamber: mirror spacing = 0.302 m , radius of curvature = 0.9144 m, number of passes = 30 and total path length = 9.06 m. The input ray is injected through the aperture in the left mirror and after 30 passes the beam exits the cell through the same aperture.
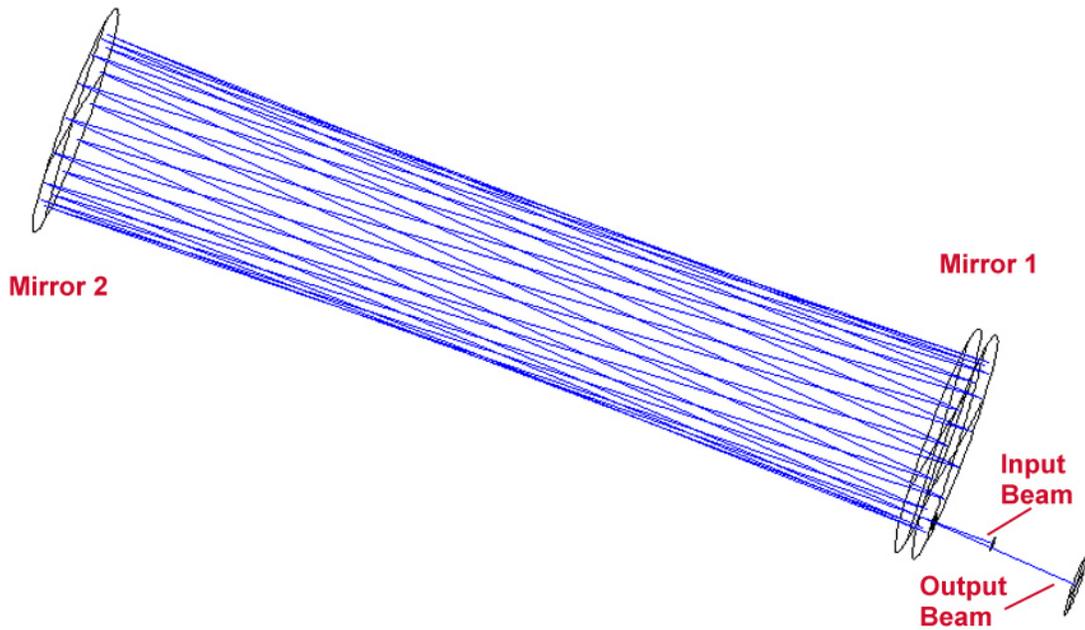
Figure 6. Ray trace of Herriott cell generated using Zemax™ optical design software. Mirror spacing=0.302 m, radius of curvature=0.914 m, n=30 passes, total path length=9.06 m.

The method used to determine the amount of scattered light reaching the exit aperture as a function of position along the beam is described as follows. The beam path is unfolded and the system is modeled as a series of 30 sequential mirrors. At the entrance pupil 37 rays are launched, which define the diameter and divergence of the incident beam. The direction of these rays changes each time a ray intersects one of the mirror surfaces until all of the rays of the incident beam escape the cell through the exit aperture on the thirtieth pass. A plane representing the position of the scattering particles is stepped along the unfolded beam path in 900 steps. At each of the 900 steps, the position of the 37 initial rays is recorded. Then at each of the 900 steps, for each of the 37 rays, a cone of 10 rays, with a cone angle varying from 0.1° to 10° in 0.1° increments, is traced through the system. The number and direction of the rays reaching the exit pupil for each of the angles is recorded. The fraction of scattered light collected for a fixed angle is determined by dividing the total number of rays reaching the exit pupil by the total number of rays launched at that angle. This calculation is performed at each of the 900 steps to determine the fraction of scattered light collected as a function of position.

Figure 7a is a plot of the fraction of scattered light collected as a function of beam position for cone angles of 0.5°, 1° and 5°. The lowest trace in this figure, showing nine spikes, represents the fraction of light scattered at 5° that exits the cell. Each of the larger spikes represents 1° and 0.5° respectively. Excluding the spike centered on a position of zero meters along the beam path, this plot shows that the exit pupil is reimaged seven times along the entire beam path. The locations of these eight images are at intervals of 1.133 m along the path. Following the plot for 0.5° along the beam path from start to finish (0 m to 9.06

m), it can be seen that the fraction of light escaping through the exit pupil has a value of 1.0 only when the position in the beam path approaches the images of the pupil. On the other hand, the fraction of light that exits the aperture is reduced to about 35% of the total incident light when the position in the beam is far away from the images of the pupil. For angles of 5°, the fraction of light exiting the aperture is zero unless the position is very near an image of the exit pupil, in which case the fraction can be as high as 0.25. On the final pass through the cell, as the exit pupil is approached (9.06 m), the fraction of scattered light collected reaches 1.0.

Figure 7b is a plot of fraction of light collected as a function of position for all angles. This function is obtained by integrating the results, for angles ranging from 0.1° to 10° in 0.1° increments, at each position. The function reaches a peak of about 0.38 at each image of the pupil until it approaches 1.0 very near the exit pupil. **Figure 7c** shows the fraction of scattered light collected as a function of angle for the entire beam path. This function, referred to as the Herriott cell output function, $H(\theta)$ is calculated by integrating the scattered light collected at all positions for each angle. This plot shows the sensitivity of the total beam path within the Herriott cell to light scattered at various angles. For a scattering angle of 2°, the fraction of light collected at the exit is approximately 0.1. At a scattering angle of 1° the value is about 0.3, and below 0.2° all of the scattered light is collected.

Figures 8a and **8b** are plots of the beam position versus fraction of light collected for an 18 pass and 26-pass cell, respectively. The parameters for these cells are given in **Table 2**. The 18-pass cell reimages the pupil three times as the beam traverses the cell, while the 26-pass cell reimages the pupil five times. The number of times the pupil is reimaged is related to the reentrant parameter, K, with the relationship,

$$\# \, pupil \, images = 2K\text{-}1. \qquad (7)$$

The value of $H(\theta)$ for the 18 pass, 26 pass, and 30 pass Herriott cells is plotted in **Figure 8c**. Upon comparing the three curves for $H(\theta)$, the 26 pass cell is slightly better than the 18 pass and 30 pass at rejecting scattered light. The path length is also much longer for the 26 pass cell (8.29 m) compared to the 18 pass cell (5.27 m).

2.2.1.2 Dependence of Scattered Light Collected on Drop Size and Wavelength

The next step of the modeling process involved incorporating the results from Mie theory with the calculated Herriott cell output function to determine the response of the extinctiometer to different drop size distributions.

The total flux of the light scattered by a drop is given by Liou (1980),

$$f_{total} = \int_0^{2\pi}\int_0^{\pi} F(\theta,\phi)r^2 \sin\theta d\theta d\phi \qquad (8)$$

$$F(\theta,\phi) = \frac{F_0}{k^2 r^2}\left[i_2(\theta)\cos^2\phi + i_1(\theta)\sin^2\phi\right] \qquad (9)$$

where $i_1(\theta)$ and $i_2(\theta)$ are the perpendicular and parallel intensity functions calculated using Mie theory. F_0=1 (unit incident amplitude), r is the drop radius, and $k=2\pi/\lambda$, where λ is the wavelength of the incident light.

2.2.2 Convolution of Herriott Cell Geometry with Scattering Theory

The amount of scattered light collected by the Herriott cell for a specific drop size and wavelength is then

$$f_{collected} = \int_0^{2\pi}\int_0^{\pi} H(\theta)F(\theta,\phi)r^2 \sin\theta d\theta d\phi \qquad (10)$$

where $H(\theta)$ is the function plotted in **Figure 8c**. The fraction of scattered light collected by the Herriott cell is

$$FractionCollected = \frac{f_{collected}}{f_{total}} \qquad (11)$$

Figure 9a is a plot of drop diameter vs. fraction of total scattered light collected at each of the nine center wavelengths used by the extinctiometer, for the 30-pass cell. A perfect measurement of the extinction of light by a drop would result in not collecting any of the forward-scattered light. The fraction of scattered light collected at all channels would be zero at all particle diameters. However, any forward collection system will receive some of the forward-scattered light. In the case of the Herriott cell, the light received at the detector is a function of scattering angle and position along the incident light beam in the cell. It can be seen in **Figure 9a** that the fraction of light collected increases with shorter wavelengths for a fixed drop size and for larger drop diameters at a fixed wavelength. This result is due to the fact that larger drops concentrate a higher percentage of scattered energy into the forward diffraction peak when compared to smaller drops.

Figure 9b is a plot of drop diameter vs. fraction of total scattered light collected for the 26 pass cell. The curves have the same general shape of those

in **Figure 9a**. A comparison of these two plots shows that the 26 pass cell does a more effective job of rejecting forward-scattered light when compared to the 30 pass cell. Based on these results, the geometry for the 26 pass was used for the airborne cloud extinctiometer.

2.3 Airborne Extinctiometer Instrument Design

The following section describes the detailed design and specifications for each of the instrument subsystems. Where relevant, more attention is paid to areas that required substantial consideration in the design. While the sequence of the work performed in Phase II did not actually occur in the order presented in this section, the final design is presented here to aid in understanding of how the instrument functions. In **Section 2.4** the testing phases of the instrument development effort are discussed. Although the initial two testing stages in **Section 2.4** were performed with intermediate instrument configurations, the information in this section will provide the necessary background for the reader to understand the purpose and sequence of the tests.

Figure 10 is a functional diagram for the airborne extinctiometer. The sample head contains the Herriott cell, wetless apertures and "cloaking cylinder". The cloaking cylinder is used to occasionally prevent the flow of cloud particles into the sample volume during extended flight through clouds. This allows signal from the incident light beam to be measured during flight to compensate for any optical contamination or long term optical drift. The sample head is the only part of the instrument exposed to the free air stream. The internal instrument components are packaged into a cylindrical form factor that slides into a standard Particle Measuring Systems (PMS) canister, typically found on research aircraft.

2.3.1 Optical Design

The optics in the airborne cloud extinctiometer have been divided into three primary subsystems: the transmitting optics module, the Herriott cell and fiber coupling optics, and the receiving optics module. Light is transmitted between the modules via fiber optics. There are substantial benefits of using fibers compared to conventional optics. A significant advantage of using three independent modules linked by fibers is that optical alignments do not have to be mechanically rigid over long distances. The use of mirrors to steer the light through the structure is eliminated. The areas of critical alignment, where light is coupled into and out of fibers, are designed to maintain opto-mechanical stability independent of the rest of the structure. Finally, each of the modules can be removed from the instrument and aligned independently.

Transmitting Optics

Figure 11 is a functional diagram of the transmitting optics module. The extinctiometer uses a Quartz Tungsten Halogen (QTH) light source to provide a broad band source to cover the nine spectral channels. The beam from the QTH

lamp is collimated and passed through a chopper wheel. A spherical reflector is placed behind the QTH lamp to redirect light emitted from the rear of the source.
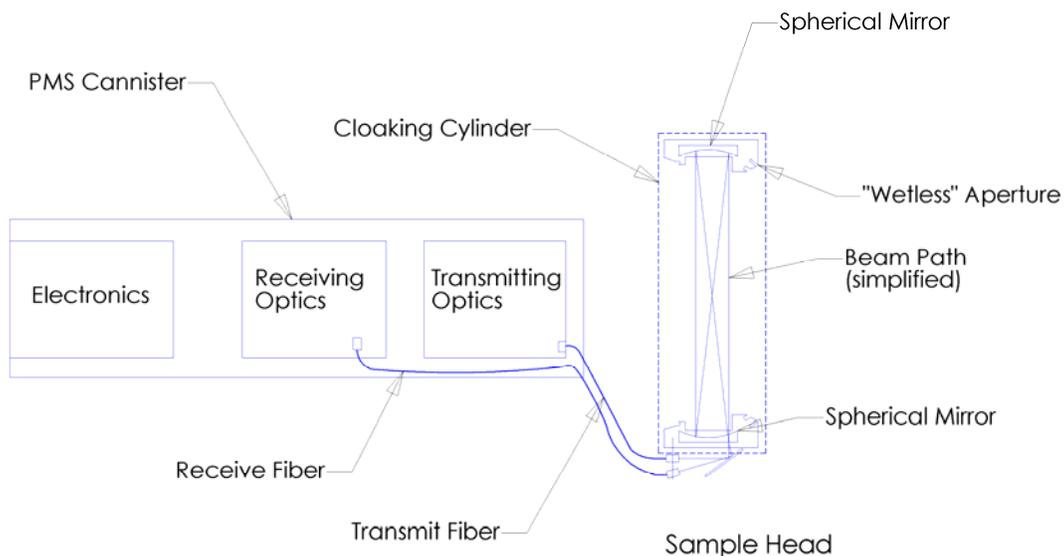

Figure 10. Functional layout of extinctiometer subsystems.

This reflector reimages the light through the filament to increase the power in the collimated output beam.

The collimated beam intercepts a beamsplitter, where 4% of the chopped beam is split off and focused onto the reference detector. The reference detector is a silicon photodiode whose output is fed to the lock-in amplifier to obtain the phase information used to extract the signal from the other detectors. The frequency of the chopper and the power output from the source are controlled using the reference signal. The signal from the reference detector is also used to normalize the signals from the other detectors and cancel out unwanted variations in the extinction measurement due to power fluctuations from the source. The reference detector uses a 950 nm optical filter with the same bandwidth as Channel 6 (**Table 1**). Therefore, the power fluctuations due to the variance in the source power are perfectly normalized out in Channel 6.

After striking the beamsplitter, the remaining 96% of the beam is coupled into a 200 μm core multimode fiber. The fiber is constructed from a silica core and silica cladding for a transmission of better than 95% per meter for wavelengths ranging from 400 nm to 2.2 μm. An aspheric lens is used at the output of this

fiber to provide a beam with 4.5 mm diameter and a divergence angle of 1.5°. The beam is then injected into the Herriott cell. The diameter and divergence of
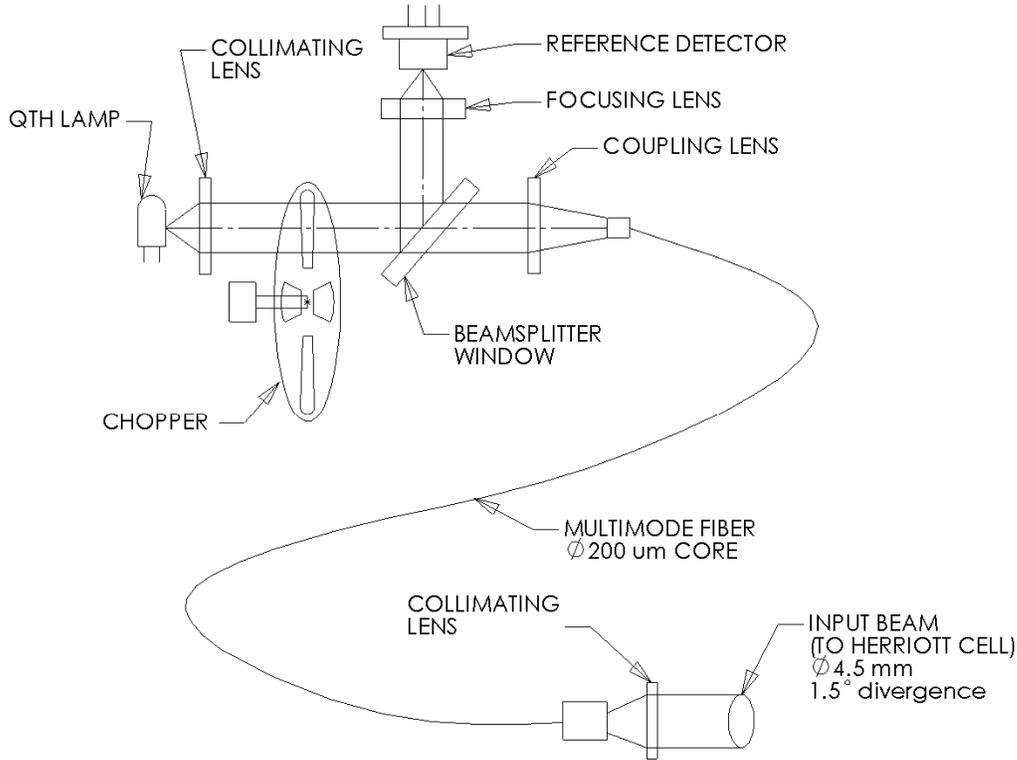

Figure 11. Transmitting optics module functional diagram.

the input beam to the Herriott cell can be changed if necessary to allow for a smaller beam size or a less divergent beam. The tradeoff for a smaller beam or a beam with less divergence will be a loss of power coupled into the fiber.

Figure 12 is a photograph of the transmitting optics module. The various components described above can be seen in the photograph. The module can be removed from the instrument by simply removing the electrical connections, mounting screws and transmitting fiber. The module is aligned outside of the instrument. After alignment, all adjustments are locked down and the module is reinstalled.

Sample Head Optics

Herriott Cell Geometry

As mentioned in **Section 2.2.3**, a 26-pass Herriott cell is used in the airborne extinctiometer. The mirror radius of curvature is 1.27 m, the separation is 0.319 m and the total path length is 8.29 m. Given the input beam dimensions into the

Herriott cell of 4.5 mm diameter and 1.5° divergence, a ray tracing analysis showed that the smallest clear aperture that could be reasonably accommodated is 4.44 cm (1.75 inches) diameter. The beam is injected into the cell through a .25" diameter hole in the input mirror radially located at 0.875". The reflected spots trace a circle of 1.75 inches diameter to most efficiently utilize the clear aperture of the mirror. Wetless apertures are used to keep the mirror surface free from contamination at aircraft speeds. **Section 2.3.2.1** further discusses the wetless apertures and their impact on the mirror clear aperture.

The spherical mirrors are Pyrex substrates with a protected Silver coating. Pyrex has been chosen for its relatively low coefficient of thermal expansion. Silver is used for the coating due to its high broadband reflectance from 0.4µm to 2.2µm. The coating consists of three layers: chromium, silver, and aluminum oxide. The layer of chromium is deposited first to promote adhesion between the vacuum deposited silver and the Pyrex substrate. The aluminum oxide serves as a protective overcoat to increase the survivability of the silver. The aluminum oxide layer is deposited using an ion beam assisted vacuum deposition process to promote tighter packing of the molecules and fewer gaps in the material, thereby increasing the durability of the coating. The aluminum oxide overcoat provides good resistance to water and high humidity and can be easily cleaned.

Fiber Coupling into Herriott Cell

In general, the angular separation between the input and output beam angles decreases as the mirror aperture decreases. The separation distance between the input and output beams also increases as the distance on the input side of the first mirror increases. The prototype instrument tested in the cloud chamber (discussed in **Section 2.4.1**) had a mirror clear aperture of approximately 2.5 inches. The beam separation was large enough to use a lens at the end of each fiber to couple the beam out of the transmit fiber and into the receive fiber. In the airborne instrument, decreasing the clear aperture of the mirrors to 1.75 inches decreases the angular separation between the input and output beams. A result of the decreased angular separation is that both beams overlap each other and cannot be spatially separated.   Furthermore, due to the refocusing of the beam by the spherical mirrors, the output beam is rapidly diverging as it exits the cell. At a distance where adequate spatial separation exists, the collection lens would require an extremely large aperture to capture the diverging beam.

To overcome these problems, a novel approach for coupling the beams in and out of the Herriott cell using a single lens and two fibers has been developed. Using a single lens, the input beam from the transmitting fiber can be "collimated" (it will still be slightly diverging) and the output beam can be focused down onto the receiving fiber. **Figure 13** is a detailed drawing of the Herriott cell to fiber coupling mechanism designed to hold and position the fibers at the correct angles and distances. Both of the fibers are potted into the fiber optic positioner. The positioner is then adjusted to place the face of the fibers at the focal length of the lens. The fiber coupler retaining barrel is then positioned with respect to the Herriott cell to inject the beam at the calculated angle to satisfy the reentrant

condition. This arrangement results in a compact sampling head with the least amount of volume being necessary behind the Herriott cell input mirror.
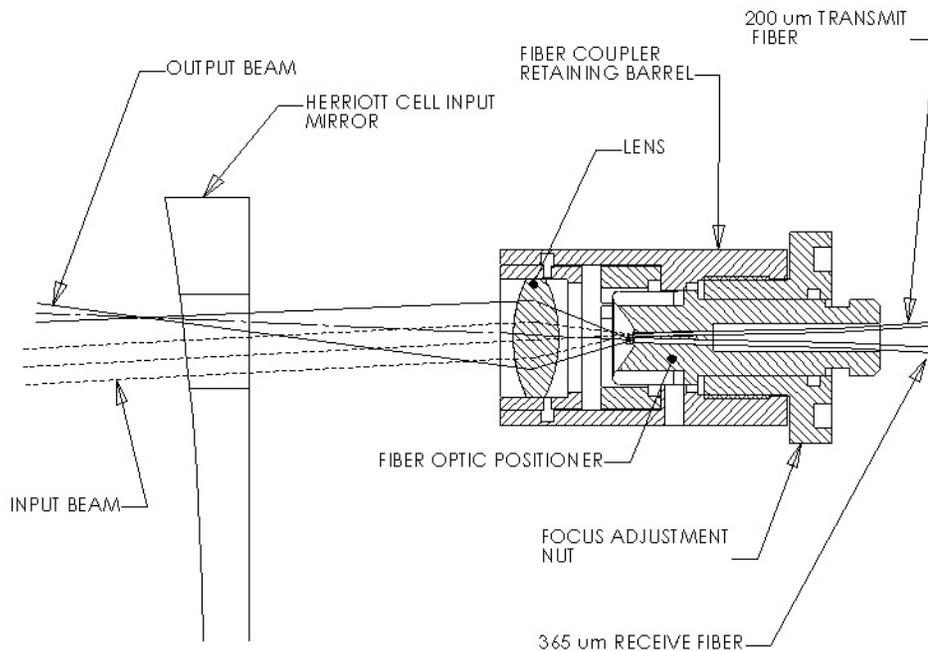

Figure 13. Herriott cell to fiber coupling assembly**.**

Receiving Optics

Figure 14 is a functional drawing of the receiving optics subsystem. Using the same aspheric lens to collimate the input beam, the light exiting the Herriott cell is coupled into a silica / silica multimode fiber with a 365 μm core and directed to the receiving optics system. A collimating lens is used at the fiber output to produce an 8 mm diameter beam with minimum divergence. The collimated beam is then split and directed to three detectors that measure the extinction coefficient over 9 spectral channels. As mentioned previously, **Table I** is a list of the nine spectral channels that can be detected by the extinctiometer.

Custom made dielectric beamsplitters are used to separate out the wavelengths that go to each detector. It is desirable to reflect the shortest wavelengths first because dielectric stacks designed to reflect long wavelengths and pass short wavelengths have harmonics in the reflectance bands at shorter wavelengths, but not at longer wavelengths. The reflectance and transmittance at the wavebands of interest is optimized if the shorter wavelengths are reflected and longer wavelengths transmitted.

The collimated beam is first split at beamsplitter #1, where wavelengths from 0.4 – 1.0 μm are reflected to a filter wheel with six filters. A silicon photodiode measures the signal transmitted through these filters. The six filters, corresponding to Channels 1-6, have center wavelengths of 450 nm, 550 nm, 650 nm, 750 nm, 850 nm and 950 nm. Each of these filters has a bandwidth of

70 nm. The bandwidth is measured at the wavelengths where the full width half maximum (FWHM) point occurs; i.e., the wavelengths at which the filter transmittance is 50% of the peak transmittance.

Wavelengths from 1.1 μm to 2.3 μm are transmitted by beamsplitter #1. These wavelengths are directed to beamsplitter #2, where wavelengths from 1.2 μm to 1.8 μm are reflected to a filter wheel containing two filters centered at 1.375 μm and 1.64 μm for Channels 7 and 8, respectively. Channel 7 has a bandwidth of 30 nm and Channel 8 has a bandwidth of 25 nm. An extended InGaAs thermo-electrically (TE) cooled detector, which detects wavelengths out to 1.9 μm, measures the extinction from Channels 7 and 8. A rotating filter wheel is used to switch these two filters in and out of the beam path.

Wavelengths from 1.9 to 2.4 μm are transmitted by beamsplitter #2. The beam next intersects the filter for Channel 9 with a center wavelength at 2.13 μm and a bandwidth of 50 nm. Another extended InGaAs TE cooled detector, sensitive at wavelengths out to 2.6 μm, continuously samples the signal for Channel 9.
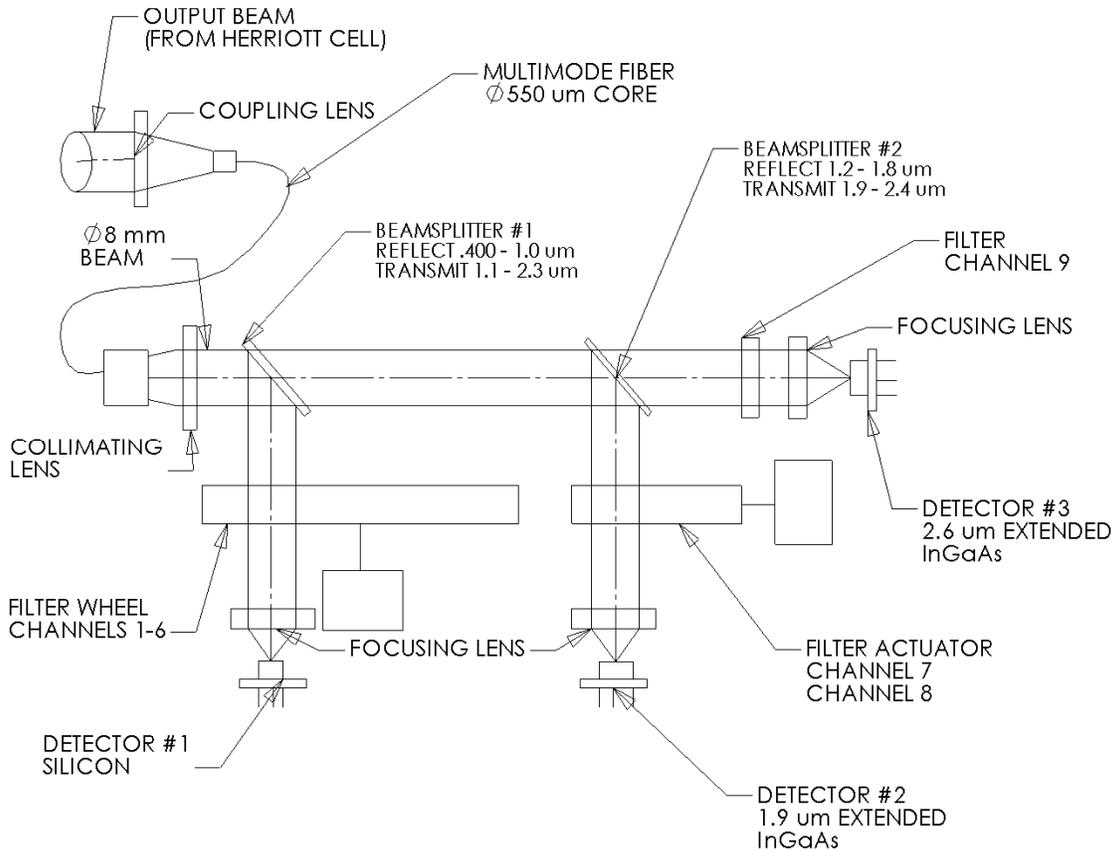

Figure 14. Receiving optics module functional diagram.

Figure 15 is a photograph of the receiving optics module. Similar to the transmitting optics module, the alignment for this unit is performed outside the instrument. After the alignment is completed, the adjustments are locked down and the unit is reinstalled in the extinctiometer.

2.3.2 Mechanical Design

The mechanical components for the extinctiometer are divided into two main parts: the sample head and the internal components. The following sections describe the mechanical design and packaging concerns for the extinctiometer. Computational fluid dynamics (CFD) simulations were performed to aid in aspects of the design involving airflow around and through the instrument. Results from the CFD simulations are also presented.

2.3.2.1 Sample Head Design

Optical Bench

The sample head for the airborne cloud extinctiometer consists of the optical bench, the outer cloak tube, the cloak actuating mechanism, and the sample head support structure. This part of the instrument is exposed to the free air stream to allow cloud particles to pass freely through the optical path of the Herriott cell, where the extinction measurement is made. The optical bench is designed to act as the Herriott cell structural support**.**

Figure 16 is a Solidworks™ cross-sectional view showing the primary components in the optical bench. The optical bench consists of a slotted tubular support, two wetless apertures/ mirror mounts, the two Herriott cell mirrors, the fiber-to-Herriott cell coupling barrel and the associated opto-mechanical alignment stages to correctly position the fiber coupling barrel. The transmit and receive fibers are permanently attached to the optical bench. The fibers pass through a sealed bulkhead fitting between the sample head and internal instrument components to couple the transmitting and receiving optics modules with the optical bench. The optical bench can be removed from the sample head by disconnecting the fibers from the optics modules and passing them through the bulkhead fitting. This allows the optical bench to be aligned outside of the instrument.

Figure 17 is a photograph of the optical bench removed from the instrument during a preliminary evaluation. The cylindrical tube is made from Amalgon, a fiberglass composite material chosen for its excellent stiffness to weight characteristics. High stiffness is necessary to maintain the alignment of the Herriott cell mirrors. The mirrors mount in the wetless apertures, which then slide into the tube with a light press fit. This design ensures the mirrors are on the same optical axis, collinear with the axis of the tube, and remain parallel to each

other. Calculations were performed that show the aerodynamic loading on the tube will not produce appreciable deformation resulting in mirror misalignment.

A rectangular slot is machined into the tube to expose the Herriott cell sample volume to the external airstream. Delrin filler strips were used in the tube to occupy regions outside the rectangular slot and constrain the airflow to an area within the beam path. The optical bench is held in the support structure by concentric O-rings on each end. This type of mount allows mechanical and thermally induced stresses acting on the support structure to be de-coupled from the optical bench.
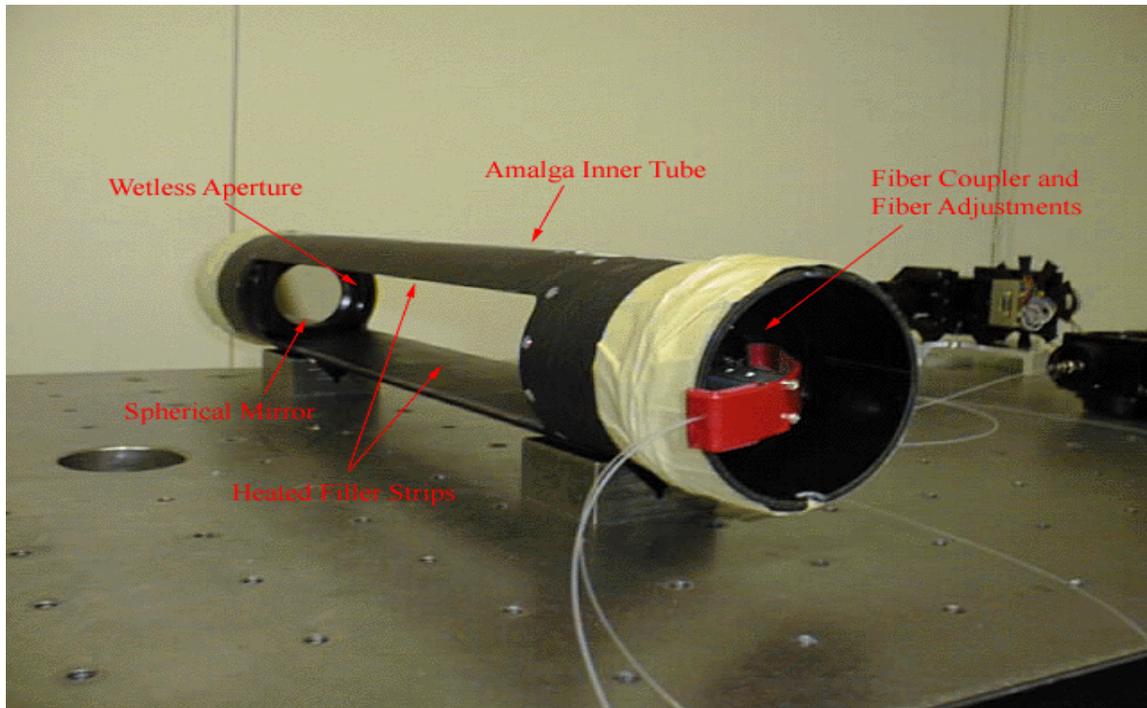

Figure 17. Extinctiometer Herriott Cell / Optical Bench

Substantial development has gone into the design of the wetless apertures. The airborne extinctiometer will be flown through clouds and a variety of meteorological conditions. The wetless apertures are used to prevent contamination, in the form of water drops, from depositing on the Herriott cell mirrors and attenuating the baseline light levels. Over the course of the last several years, SPEC has developed an aperture that is intended to keep cloud drops from wetting optical surfaces. This design was used as a starting point for the design of the apertures used in the airborne cloud extinctiometer.

Computational fluid dynamics (CFD) simulations were used as a primary design tool to assist in the design of the wetless apertures and sample head geometry. As part of the subcontract to NCAR, Dr. Cynthia Twohy performed the CFD simulations. **Figure 18** is a drawing of a wetless aperture used previously by SPEC (Lawson and Blyth 1998). The optical element (a spherical mirror in the case of a Herriott cell) sits behind the clear aperture. Two grooves around the circumference of the clear aperture divert water streaming along the surface

away from the optic. The top surface has a slope of 7.5° to inertially separate drops from the airflow by creating an aerodynamic shadow zone over the aperture.

The pictured geometry has been modified to accommodate the clear aperture for the Herriott cell beam pattern. As mentioned previously, ray tracing results were used to determine this clear aperture. To accommodate the larger clear aperture, the dimensions in the drawing have been scaled up by a factor of two and the clear aperture is circular instead of elliptical. Flow modeling has been performed to calculate drop trajectories past this aperture. A computational fluid dynamics (CFD) program called Star-CD™ has been used to perform the simulations. Star-CD™ is a multi-purpose CFD analysis code containing mathematical models of a wide range of thermofluids phenomena. For a first approximation, the aperture has been inset in an airfoil shape to insure attached flow just upstream of the aperture. The grid consisted of 29,000 elements of various sizes, with a higher concentration of small grid elements bordering the aperture.

Figure 19 shows a two dimensional model of the "wetless" aperture and airfoil in a fully developed flow field. The two dimensional cross-section is taken along the centerline of the aperture, in a plane which is parallel to the direction of flow. The free stream velocity is 150 m/s and the pressure is 204 mbar corresponding to an altitude of 40,000 ft. Velocity vectors are plotted as arrows. The direction of the arrows indicates the direction of flow and the arrow color is proportional to the velocity.

Figure 20 is a close up view of flow past the aperture. As the flow hits the aperture it is deflected upwards. The flow separates near the beginning of the clear aperture and a recirculation zone is formed in this separated region. The velocity reaches a maximum of about 20 m/s in the recirculation zone. **Figure 21** is a plot of the droplet trajectories for 10 μm water drops injected into the flow field upstream of the aperture. The solid lines represent the droplet trajectories. It can be seen that the drops are deflected upwards and over the clear aperture. The simulation shows that 10 μm drops are not entrained by the recirculation. This indicates that the spherical mirror behind the clear aperture may stay free of contamination for the indicated set of conditions. **Section 2.4.2** describes testing of the sample head in a wet wind tunnel to determine the effectiveness of these apertures

Support Structure

Figure 22 is a photograph of the extinctiometer sample head. The design of the support structure was a cooperative effort between SPEC and the NCAR Design and Fabrication Services. Most of the mechanical parts for the extinctiometer were manufactured at NCAR Design and Fabrication Services. The support structure is used to mount the optical bench and cloaking system and provides an interface between these components and the internal instrument components. The entire sample head structure is joined to the internal can

structure through the transition piece. The transition also bolts to the PMS can and acts as the load bearing structure for the sample head.
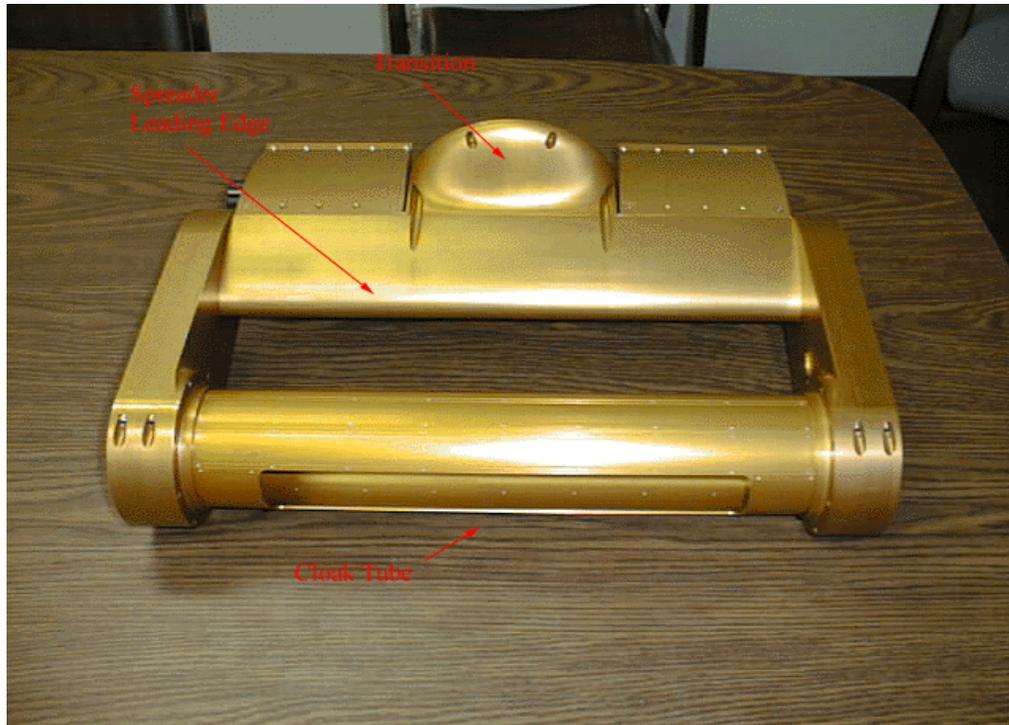

Figure 22. Extinctiometer Sample Head

CFD simulations were performed to determine the geometry of the transition piece and to determine the length of the support arms that hold the optical bench. **Figures 23a-c** are plots of the CFD results for flow through the optical bench and two different transition piece geometries. The results are for two-dimensional simulations using a cross-section down the centerline of the instrument in a plane which is parallel to the direction of flow. **Figure 23a** shows flow through the optical bench and a triangular transition piece with a separation of 13.2 cm between the two parts. **Figure 23b** shows results for the optical bench and an airfoil shaped transition piece with a separation of 9 cm. The goal of comparing these two geometries was to determine the effect of the pressure wave, caused by the transition piece, on the flow through the optical bench. The free stream velocity in these simulations is approximately 135 m/s (yellow arrows). The velocity around the slotted cylinder increases while the velocity through the slot drops to approximately 100 m/s. The pressure wave created by the transition pieces is indicated by the limits of the red arrows between the optical bench and the transitions. The flow through the slot in the optical bench looks virtually identical for each of the transition piece geometries. **Figure 23c** is a close-up view of flow through the optical bench. The average velocity through the sample volume is lower than the freestream velocity.

Based on these results, the pressure wave created by the transition pieces has an effect on the flow through the sample volume. In order to minimize this effect, the separation between the sample volume and transition piece should be selected to place the optical bench out of the pressure wave. However, this distance is limited in practice by considering the maximum allowable bending moment created by cantilevering the sample head off the front of the PMS canister. A distance of 9.5 cm was used to separate the two components and the airfoil shaped design was used. **Figure 23b** shows the airfoil shaped-spreader leading edge and the transition. The simulations are for the plane down the centerline of the instrument. It can be seen in **Figure 22** that the transition is located behind only a portion of the sample volume, and the geometry forms a complete airfoil near the ends of the spreader leading edge. Therefore, the average velocity through the sample volume is probably higher than predicted by the simulations, because the airfoil shape will have a much smaller pressure wave associated with it compared to the transition. Flow measurements in a wind tunnel or a three-dimensional CFD simulation would be necessary to accurately predict the velocity at different points in the sample volume.

Cloaking System

The cloaking system has been designed to measure the background light levels while flying through cloud. A change in background signal levels may be due to contamination on the mirrors or transmitting optics.   The cloaking system blocks the flow of cloud particles into the sample volume by rotating a slotted outer cylinder around the inner cylinder of the optical bench.

Figure 24 shows the details of the drive mechanism for the cloak tube. The cloak tube is supported by bearings on both ends and rotates ninety degrees when driven by the double acting pneumatic cylinder. Disposable CO_2 cartridges are used to power the pneumatic system.   The force is transferred from the cylinder to the drive gear and then the actuating gear to rotate the tube. Heaters are installed on the cloak tube for deicing purposes and to prevent ice from forming between the cloak tube and the optical bench, thereby preventing the tube from rotating.

Figure 25 shows the location of the CO_2 cartridge chamber and other pneumatic components. The CO_2 cartridge can be replaced with the instrument mounted on the aircraft in the PMS can.   The black delrin cap shown in the photograph is used to access to the CO_2 chamber and replace the cartridge. A new cartridge is inserted and as the cap is tightened, the cartridge is sealed and then punctured, pressurizing the system. The CO_2 undergoes a 750:1 volumetric expansion when going from a liquid to a gas. The regulator is used to reduce the 590 psi output pressure of the cartridge to 100 psi line pressure. The chamber is heated to maintain the output pressure from the CO_2 cartridge. The valve is toggled on and off by computer to actuate the cloak. A pressure transducer is used to monitor the line pressure and alert the user when the CO_2 cartridge needs to be replaced.
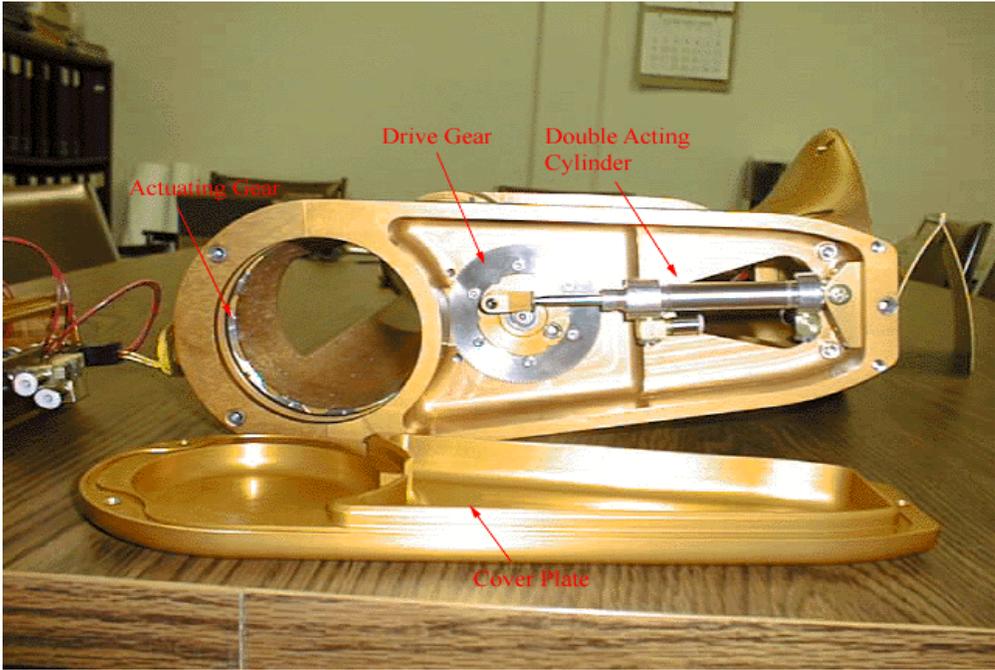
Figure 24. Details of drive mechanism for cloak tube**.**
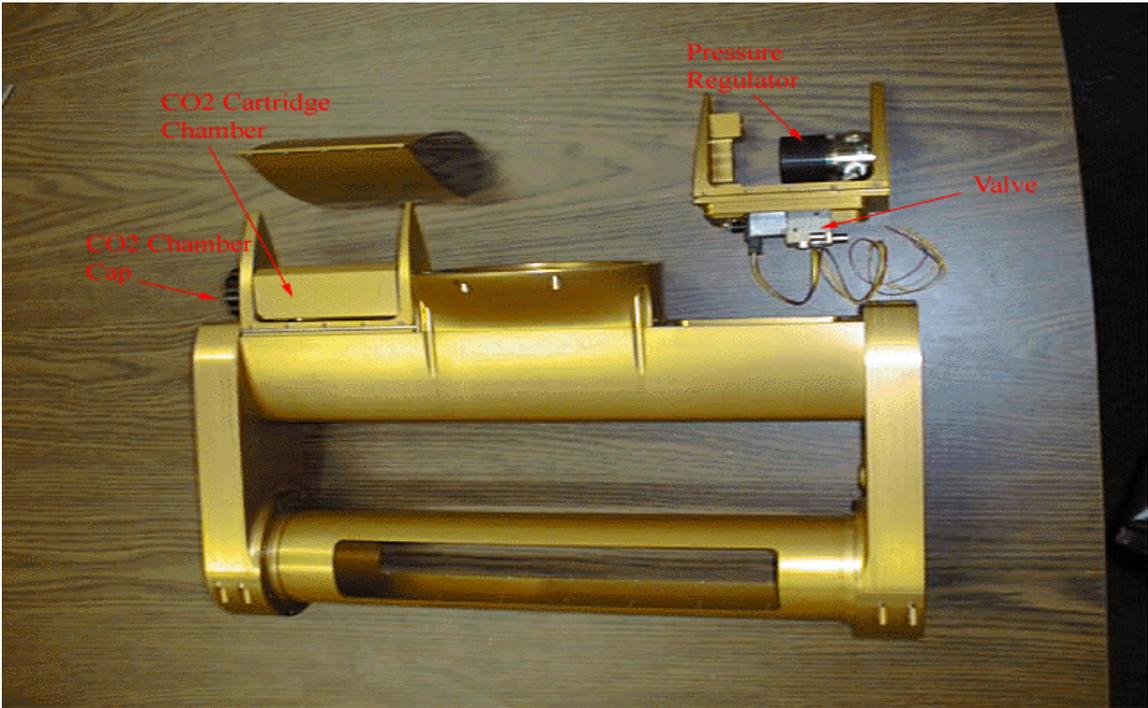

Figure 25. Location of cloaking system pneumatic components.

2.3.2.2 Internal Instrument Components

The internal support structure fits inside a PMS can and supports the transmitting and receiving optics modules, power supplies, electronics card cage and various other internal components. All of the design and packaging of the internal components was done using Solidworks™ 3-D solid modeling software. A number of packaging scenarios were investigated in Solidworks™ to arrive at a final design that was spatially efficient and functional, given the large number of internal components. **Figure 26** shows the final Solidworks™ layout for the airborne extinctiometer.

Figure 27a shows the optics modules and electronics card cage mounted into the internal support structure. The electrical connector, shown on the right side of the photo, mates with the aircraft connector as the instrument slides into the PMS can. The serial data transmission lines and instrument power lines pass through this connector. The front bulkhead plate, also seen in **Figure 27a**, attaches to the transition on the sample head. The fibers mount through the front bulkhead plate in a removable fitting and carry light between the sample head and the inside of the can. A bulkhead electrical connector is used to pass electrical signals between the sample head and internal components. Disconnecting the fibers and the electrical connector allow the sample head to be completely separated from the internal instrument components. **Figure 27b** is a side view of the internal structure.   The power distribution board is visible below the transmitting optics module.   The bottom view of the internal components is shown in **Figure 27c**. The EMI line filter is mounted on the bottom right and the stepper motor controller boards, used to actuate the filter wheels, are mounted on the left.
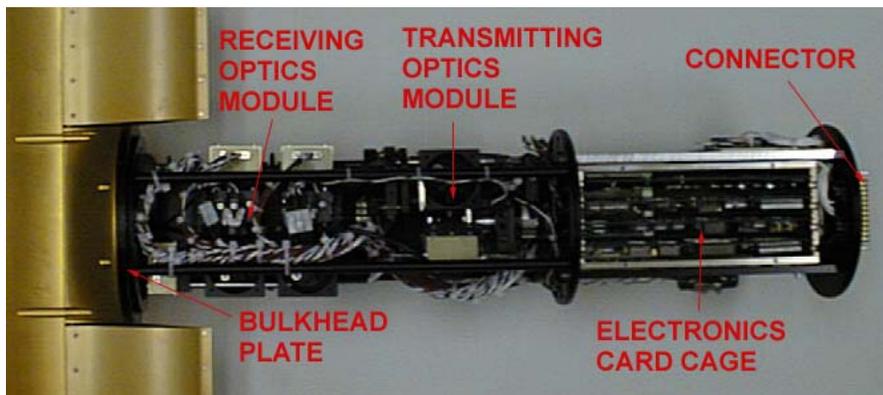

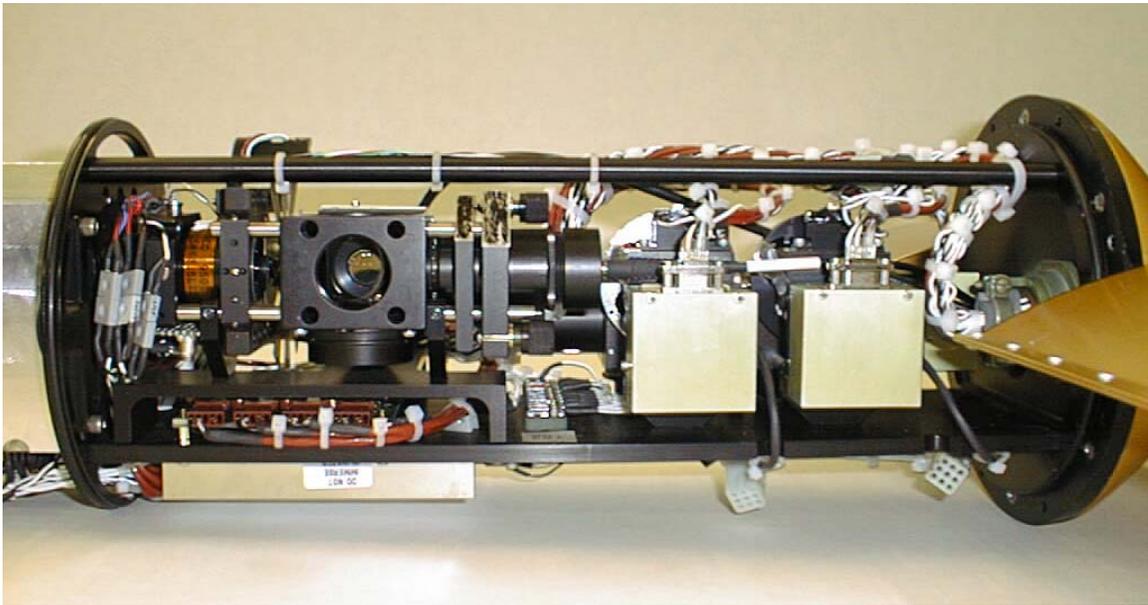
Figure 27a. Photograph of internal instrument components**.**

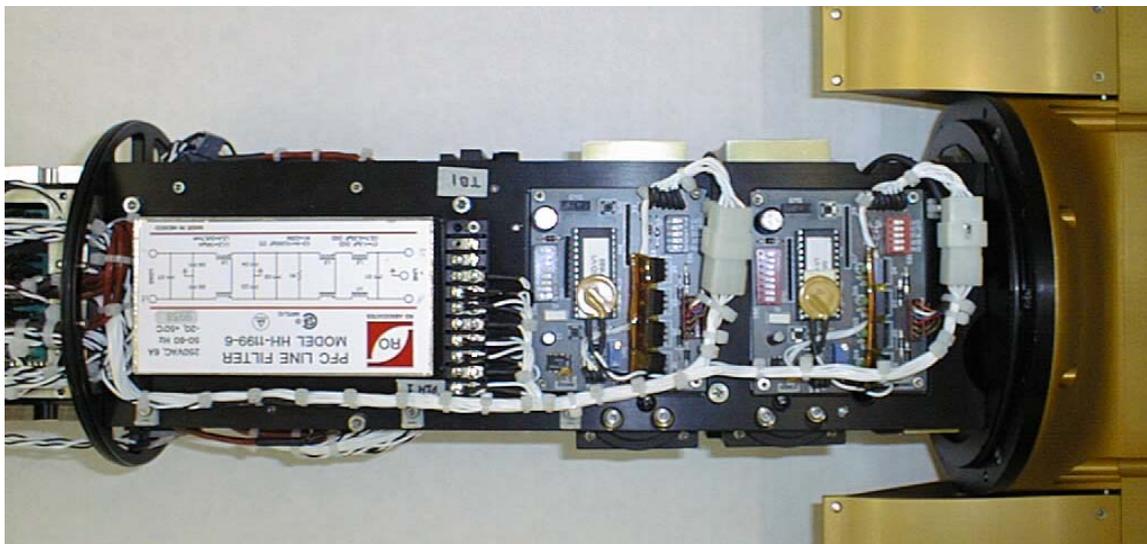**Figure 27b.** Side view of internal components.

Figure 27c. Bottom view of internal instrument components.

2.3.3 Electronics Design

The extinctiometer electronics are handled with a set of proprietary printed circuit boards (PCB). **Figure 28** shows a block diagram of the extinctiometer electronics. The majority of the electronics are housed in a card cage for compactness and heat conservation. This cage contains all of the cards except the detector preamplifier cards and the stepper motor controller cards. **Figure 29a** is a photograph of the electronics card cage and cards installed in the instrument. **Figure 29b** is a photograph of the cards removed from the cage. The cards are a proprietary format that utilizes two edge connectors per card. One connector is used to bus signals between cards while the other is used to
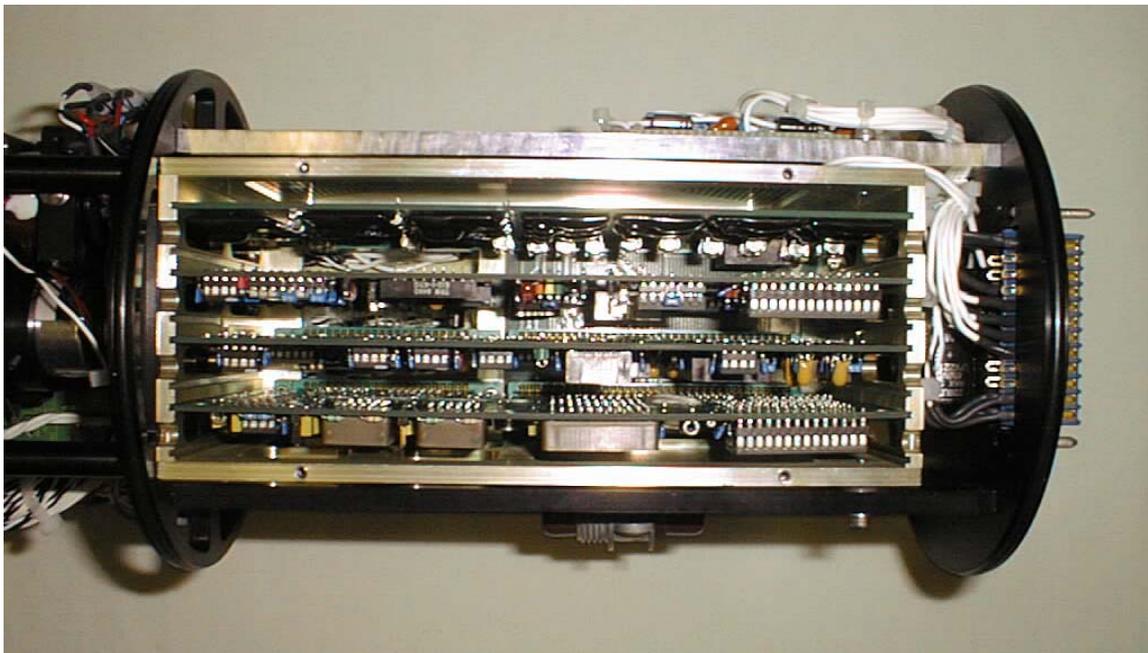
Figure 29a. Electronics card set in card cage.
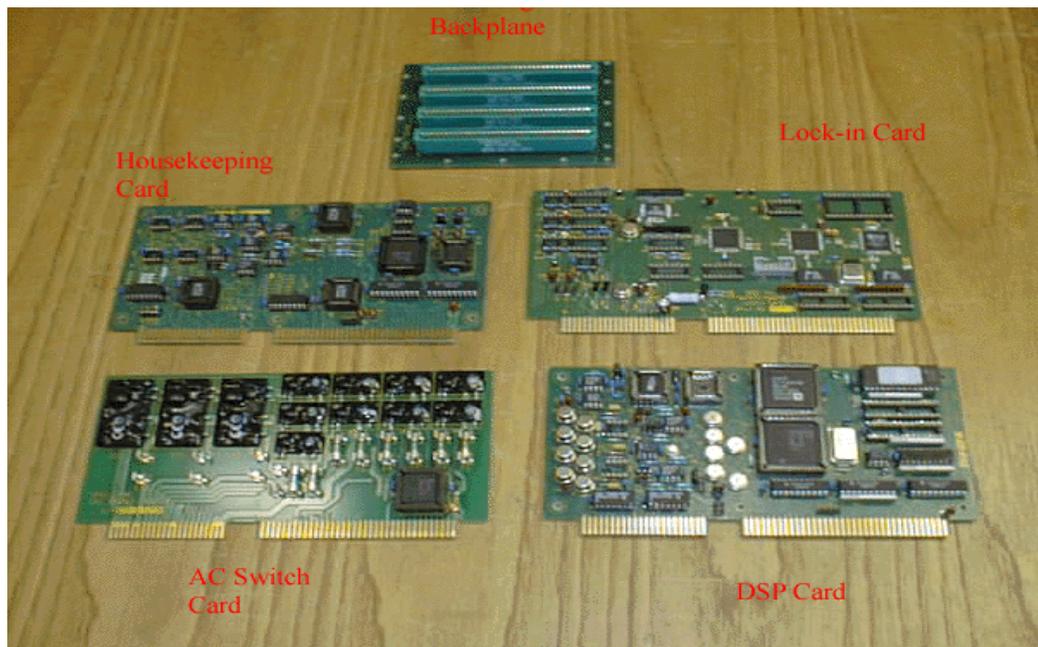

Figure 29b. Electronics card set and backplane.

bring discrete signals to a card. They communicate with a personal computer via an established synchronous serial interface.

The electronic components for the airborne cloud extinctiometer consist of the photodetector amplifiers, the chopper motor, the filter array and cloak actuators,

the set of PCBs which reside in a backplane-bussed card cage and the DC power supplies.

Electronics - Theory of Operation

The extinctiometer delivers a modulated light beam to a multipass measurement cell. The light beam is then coupled out of the cell, spectrally separated, and directed to three different detectors. Spectral filters are used in front of each detector to further isolate the wavebands of interest. Synchronous detection with a lock-in amplifier is used to measure the attenuation of the modulated light beam in the Herriott cell. The lock-in amplifier greatly increases the signal to noise ratio, resulting in an improvement of the minimum detectable extinction coefficient.

The light source is a six watt QTH lamp that is collimated and passed through a rotating chopper wheel. This wheel has 10 slots in it and is operated at 6000 revolutions per minute resulting in a modulation frequency of 1000 Hz. Four percent of the chopped beam is passed to the reference detector, to monitor the frequency and amplitude of the outgoing beam. The frequency of the modulated beam is used to continuously servo the chopper motor frequency to 1000 Hz and to provide phase and frequency input to the lock-in amplifier. The amplitude of the outgoing beam is monitored by a digital servo, maintained by the system DSP, to keep the lamp output at constant power.

Detectors were selected based on having the highest D* (a measure of the responsivity and noise^{-1}) in each of their respective wavelengths. All four detectors are photodiodes, allowing the same preamplifier to be used for each detector with a different gain resistor. Detectors 2 and 3 each contain a Thermo-Electric-Cooler (TEC) and a thermistor to maintain the detectors at a stable operating temperature and decrease noise.

The power supplies are high-density AC/DC switcher units. Although these supplies are slightly noisier than linear supplies, the noise is uncorrelated with the modulated light beam and will be rejected by the synchronous detection. The gains in power efficiency and size outweigh the noise.

2.3.3.1 DSP Card Description

The DSP card utilizes an Analog Devices ADSP2101 Digital Signal Processor (DSP) to control and monitor the probe hardware. This card has a bi-directional, high-speed, synchronous serial port (RS-422 levels), 8 analog outputs and 8 medium current switches that can be used to drive heaters. The card also has 8192 16-bit words of high speed RAM and 16 K bytes of EPROM, where the program is stored and a watchdog timer is used to prevent the software from hanging.

A Programmable Logic Device (PLD) (U3) decodes the DSP's external data memory for the CPI as described in **Table 3**.

Table 3. DSP memory Map

Address	Size (words)	R/W	Description
0x0000	2	R/W	Housekeeping ADC AD7878
0x0002	2	W	Housekeeping Control Register
0x0004	1	W	System Control Register
0x0006	1	W	AC Heater Register
0x0800	0x2000	R/W	External RAM
0x3001	1	W	Near IR TEC
0x3002	1	W	IR TEC
0x3400	1	R	Lock-In FIFO
0x3401	1	R	Lock-In Control/Status
0x3402	1	R	Reference Setpoint

The DSP controls the TECs for the near IR (detector 2) and IR detectors (detector3) through 12-bit Digital to Analog Converters (DACS) which output a voltage between 0 and 2.5 V. This voltage controls power amplifiers that actually drive the TECs. An eight-bit parallel port utilizes a FET transistor to switch 12 VDC to the cloaking actuator solenoid valve.

Data are sent between the extinctiometer and the data system as asynchronous 9600-baud serial packets. Each signal is transmitted as differential TTL or RS-422. The wiring harness acts as a null modem connecting the transmitters on the probe to the receivers on the data system and visa versa. The data packet, which is transmitted from the probe, is an ASCII string that has the format which is given in **Table 4**. Note that all numbers are sent as hex ASCII with a space used as a delimiter. The parameters are 16 bit integers unless otherwise noted. The packet is sent once per second.

Table 4. Data Packet Format.

Character	Description
1-2	Packet ID "DP"
4-11	Seconds of year 32-bit integer
12-15	Command Number
17-20	Status – Bit mapped – Bit = 1 if true Bit 0 – Cloaking in progress Bit 1 – Heaters enabled Bit 2 – 15 Not used
22-25	Reference Detector DC
27-30	Reference Signal
32-35	Visible DC Level (Detector 1)
37-40	Visible Signal 1 (Channel 1)
42-45	Visible 1 Ratio (Channel 1)
47-50	Visible Signal 2 (Channel 2)
52-55	Visible 2 Ratio (Channel 2)
57-60	Visible Signal 3 (Channel 3)
62-65	Visible 3 Ratio (Channel 3)

67-70	Visible Signal 4 (Channel 4)
72-75	Visible 4 Ratio (Channel 4)
77-80	Visible Signal 5 (Channel 5)
82-85	Visible 5 Ratio (Channel 5)
87-90	Visible Signal 6 (Channel 6)
82-95	Visible 6 Ratio (Channel 6)
87-100	Near IR DC Level (Detector 2)
102-105	Near IR Signal 1 (Channel 7)
107-110	Near IR 1 Ratio (Channel 7)
112-115	Near IR Signal 2 (Channel 8)
117-120	Near IR 2 Ratio (Channel 8)
122-125	IR DC Level (Detector 3)
127-130	IR Signal (Channel 9)
132-135	IR Ratio (Channel 9)
137-140	DSP Card Temperature
142-145	Housekeeping Card Temperature
147-150	Lock-In Card Temperature
152-155	Reference Detector Temperature
157-160	Visible Detector Temperature
162-165	Near IR Detector Temperature
167-170	IR Detector Temperature
172-175	Gas Chamber Temperature
177-180	Outer Cylinder Temperature
182-185	Inner Cylinder Temperature
187-190	Turbulence Fence Temperature
192-195	Can Air Temperature
197-200	Mirror Temperature
202-205	Wetless Window Aperture Temperature
207-210	Gas Pressure
212-215	+5 VDC
217-220	+12 VDC
222-225	-12 VDC
227-230	+28 VDC
232-235	Checksum
237-238	String Terminator (0x0A0D)

Two types of control packets are sent to the extinctiometer. The first is used to set the time and has the format listed in **Table 5.** The parameters in these packets are hex ASCII separated with spaces.

Table 5. Time Set Packet.

Charact	Description
1-2	Packet ID "TM'
4-11	Seconds of year (32-bit integer)
13-17	Checksum
19-20	String Terminator (0x0A0D)

The second type of packet sent by the data system is used to change control parameters in the instrument. **Table 6** lists the format of the set mode packet.

Table 6. Set Mode Packet Format.

Character	Description
1-2	Packet ID "SM"
4-7	Command Number
9-12	Control – Bit mapped – Bit = 1 if true Bit 0 – Cloaking in progress Bit 1 – Heaters enabled Bit 2 – 15 Not used
14-17	Near IR Detector Temperature Setpoint
19-22	IR Detector Temperature Setpoint
24-27	Gas Chamber Temperature Setpoint
29-32	Outer Cylinder Temperature Setpoint
34-37	Inner Cylinder Temperature Setpoint
39-42	Turbulence Fence Temperature Setpoint
44-47	Mirror Temperature Setpoint
49-52	Wetless Window Aperture Temperature Setpoint
54-57	Checksum
59-60	String Terminator (0x0A0D)

2.3.3.2 Housekeeping Card Description

The housekeeping card monitors slowly varying signals from scattered locations around the probe. It conditions signals from transducers, sensors and voltage supplies, digitizes these signals, and buffers these data for retrieval by the DSP. The card has the ability to monitor 20 temperatures, 16 from AD590 sensors and four from thermistors. The sixteen AD590 channels are biased to operate between -60° and + 60° C. The thermistor amplifiers are set up to operate from -42° to +45° C. The AD590 sensors are used to monitor heat zones throughout the probe as well as the temperature inside the can. The data packet format lists all the parameters that are sampled.

Analog housekeeping parameters are converted to digital data by a 12-bit bipolar sampling ADC that has an 8-word output FIFO and is controlled by a state machine. The state machine is started when the DSP writes the number of conversions to perform in its control register (bits 5 - 8). This number of analog channels are converted, starting with channel 0, and are buffered in the FIFO. The status register in the AD7878 may be read to determine when data are ready. After the conversions are complete, the next sub multiplexer address (control register bits 0 - 4) is output to the temperature and voltage multiplexers thereby allowing maximum settling time for the switched temperature amplifiers.

The housekeeping card appears as three registers on the DSP bus, the state machine control register, the AD7878 control/status register and the AD7878 FIFO register. The system memory map (**Table 3**) gives the exact location of these registers.

2.3.3.3 Lock-In Amplifier Card Description

The Lock-In Amplifier (LIA) card controls and samples the front end of the extinctiometer. It controls the QTH lamp intensity and the chopper wheel rotational frequency with Pulse Width Modulated (PWM) signals. Selection of the filters in the filter wheel are under control of the Lock-In Amplifier card. The most important function of the LIA card is to implement the digital Lock-in amplifiers used to synchronously detect the extinction signal.

A three channel digital lock-in amplifier is used to synchronously detect the attenuation of the light beam by cloud particles on the three detectors. Each of the three data channels differentially accepts the signal from a detector and amplifies the signal, under software control, to utilize the full range of the Analog to Digital Converter (ADC) when the probe is taking a background (cloaking). After some filtering and conditioning, each channel is multiplied by the normalized reference signal and the product is smoothed to yield three synchronously detected channels. The DSP which performs the lockin functions is an Analog Devices ADSP21060 (SHARC) that is a powerful floating point unit with a parallel interface that enables the system DSP quick access to the SHARCs memory. The system DSP reads and collates the channel data with the appropriate tags that indicate which filters are in place before sending them to the data system for recording and display. A single Programmable Logic Device (PLD) decodes devices, implements the PWM logic and acts as a receiver for the serial strings from the data system.

2.3.3.4 Power Switch Card Description

The AC switch card distributes AC power to the various heat zones of the extinctiometer. The card contains a 12-bit latch that controls 12 solid state relays. The solid state relays are rated for either 60 or 400 Hertz and AC voltages up to 280 V. Two types of relays are used for different current loads. Relays S1 – S9 are Crydom ASO242 that are rated for 2A while S10 – S12 are Crydom CX240 that are rated for 5A. Three AC circuits supply power to the card and the AC returns are isolated from the frame to prevent ground faults. Each output circuit is protected with a fuse.

2.3.4 Software Description and Design

A real time software interface for the airborne extinctiometer has been developed and tested. The code is written in Visual Basic and runs on a PC. The real time code reads and records all instrument data and allows the user inside the aircraft to control the operation of the instrument. Data is sent from the DSP card in the extinctiometer card cage to the computer serial port once a second at 9600 baud. Heater temperature set points, thermoelectric cooler (TEC) control parameters and cloaking cycles can be controlled from the software. The extinction coefficient for Channels 1-9 is calculated, recorded and displayed in real time.

Figures 30a - e are screen captures showing each of the available screens in the real time code. **Figure 30a** displays a strip chart plot of the extinction coefficient for Channels 1-9. The screen is broken into two strip charts. The top strip chart displays Channels 1-6 on Detector #1 and the bottom strip chart displays Channels 7-9 on Detectors #2 and #3. A red indicator light in the bottom right corner of the screen notifies the operator whether or not data is being recorded. The y-axis for the strip charts is user settable and the instantaneous value for each channel is displayed in a text box above the strip chart plots. The horizontal bar across the bottom of the screen displays other relevant parameters such as the Probe time, the PC time, the date, the last command number sent to the probe and whether or not a background has been taken.

Figure 30b displays the instantaneous values of the housekeeping parameters. The boxes to the right of each parameter can be checked to allow the user to plot two of the Housekeeping parameters in a strip chart on the right side of the screen. The gain and offsets for each parameter, required to convert the digital counts to engineering units such as temperature and voltage, are accessed by double clicking on a particular housekeeping reading.

Figure 30c displays the instantaneous values of the optical signal levels, the setpoint for servoing the lamp and the pwm signal used to servo the lamp. The status box in the lower left corner of the screen contains indicator lights that correspond to the operation of the various heaters. A red indicator light informs the user that a heater is being powered on or if the cloak is being actuated.

Figure 30d contains the operating setpoints for the various heater temperatures and cloaking parameters. The optical path length is also entered on this screen. Two radio buttons allow the user to initiate a cloaking cycle or take an immediate background. A cloaking cycle rotates the cloak closed for the cloak duration. The cloak sample period is the last number of seconds in the cloak duration over which the background signal levels are calculated. The "take immediate background" button does not close the cloak, but simply calculates the background signal levels for the cloak sample period. This function is used to take backgrounds in clear air without rotating the cloak. This screen also contains the check boxes used to toggle the individual heaters on and off. After the appropriate box is checked, the "send set mode packet" button is clicked. The selected heater will then be powered on and operated at the user defined set point. Going back to the previous screen will show that the red indicator light for the corresponding heater comes on. The final screen, **Figure 30e**, is used to verify serial communications between the PC and the extinctiometer. Incoming data strings are received each second in the incoming data window and commands out to the probe are displayed in the top outgoing window.

2.4 Laboratory and Flight Testing

To assist the reader in following the development and testing cycle for the airborne extinctiometer, **Table 7** chronologically lists the laboratory and flight testing phases of the research performed in Phase II. The third column lists the instrument   configuration   used   in   the   test.

Laboratory / Flight Test	Date	Instrument Configuration	Objective of Test	Result / Action	
Laboratory Stability	3/98-6/98	**Laboratory Prototype #1**: Lab Herriott cell with conventional optics and Phase I electronics	Compare Optical stability of Herriott Cell to Phase I Design	Optical Stability of Herriott Cell superior to Phase I design, proceed with Herriott cell based design	
Cloud Chamber	1/99-3/99	**Laboratory Prototype #2**: Lab Herriott cell with prototyped optics modules and fibers, modified Phase I electronics	Evaluate feasibility of Herriott cell based instrument, compare with FSSP and Transmissometer	Lab prototype performed well, qualitative comparison good, proceed with final airborne design	
Wet wind tunnel test #1	1/00-2/00	**Engineering Prototype #1**– Sample Head with final optics modules, modified Phase I electronics	Evaluate wetless aperture performance, cloak actuation, aerodynamic stability	Aerodynamic stability good, fouling of mirrors by streaming drops occurs, cloak actuates: add turbulence fences	
Wet wind tunnel test #2	2/00-3/00	**Engineering Prototype #2**-Same as above with addition of turbulence fences	Evaluate mirror fouling with addition of turbulence fences and cloak actuation	Large improvement in mirror fouling, cloak splashes drops on mirror in high LWC	
Transmissometer and mounting pylon Test Flight	3/16/00	-	Evaluate Tranmissometer performance on Lear jet, effect of newly added pylons on Learjet	Minimal effect of pylons on Learjet, Tranmissometer performs satisfactorily during level flight, but not while maneuvering	
Extinctiometer Test Flight #1	3/24/00	**Engineering Prototype #3**- Sample Head used above, integrated final electronics and internal components, final real-time software	First extinctiometer test flight, evaluate overall performance	Cloak system has pneumatic leak, extinctiometer otherwise performs fairly well, temperature dependent baseline drift observed, spectral drift of lamp observed. Data are useful	
Extinctiometer Test Flight #2	3/27/00	**Engineering Prototype #3**	Second test flight, Collect data	Fiber potting fails early in flight: Modify mechanical design for fiber potting, use epoxy instead of RTV	
Environmental Chamber Test #1	4/3/00-4/7/00	**Engineering Prototype #4**: fibers potted differently	Investigate thermal stability of instrument	Temperature dependent drift tracked to optical bench, spectral drift of lamp quantified	
Extinctiometer Test Flight #3	4/12/00	**Engineering Prototype #4**	Collect data, evaluate new potting technique	Potting technique works, temp. dependent drift still present, modify optical bench to 25 pass cell	
Extinctiometer Test Flight #4	4/26/00	**Engineering Prototype #5**: 25 pass cell, coupling out far side	Collect data, evaluate modified optical bench	Substantial improvement in thermal baseline drift	
Environmental Chamber Test #2	6/00	**Engineering Prototype #5**	Characterize thermal performance of modified optical bench	Above –25 C, thermal performance much improved, below –25 C thermal performance degraded. Cause unknown. Instrument will perform well during constant altitude flight.	

Table 7. Chronological summary of extinctiometer laboratory and flight tests.

2.4.1 Laboratory Stability and Cloud Chamber Tests

Prior to designing the complete airborne instrument described in the previous section, some preliminary tests were performed with a laboratory prototype extinctiometer. The tests demonstrated the feasibility of using a Herriott cell to make extinction measurements. A 30-pass Herriott cell was prototyped in the laboratory. The optical stability was evaluated using the source, detector and electronics from the Phase I instrument. Conventional optics were used to deliver the light to and from the Herriott cell. This instrument configuration is referred to as "Laboratory Prototype #1" in **Table 7**. Based on the superior optical stability, the Herriott cell based design was a substantial improvement over the Phase I retroreflector design.

2.4.1.1 Experimental Comparison of Prototype Extinctiometer, FSSP and Russian Transmissometer in a Cloud Chamber

The next series of tests were performed in a warm cloud chamber built at SPEC. Laboratory Prototype #2 (Table 7) used the 30-pass Herriott cell with breadboarded optics modules and fibers to couple light to the cell. The Phase I electronics were modified to add an additional detector. The extinction coefficients measured by the prototype extinctiometer were compared with the extinction coefficients measured by an FSSP and the Russian transmissometer.

Experimental Setup and Instrumentation

A "cloud" chamber was constructed from PVC pipe and flexible plastic sheet. **Figure 31a** is a photograph of the outside of the chamber. The dimensions of the cloud chamber were approximately 3' wide by 7' long by 7.5' high. A galvanized steel floor was constructed to catch excess water that would accumulate on the bottom of the cloud chamber. The source used to generate the cloud was an ultrasonic humidifier suspended five feet high inside the chamber.

As shown in **Figure 31a**, the FSSP is located approximately 18 inches above the floor with the sample tube inserted into the chamber. A small fan was used to aspirate the FSSP and draw particles through the instrument sample volume. Also seen in this photo is the initial location of the optical module for the transmissometer. **Figure 31b** is a photograph of the inside of the cloud chamber. The ultrasonic humidifier is suspended near the rear of the chamber. The Herriott cell and coupling optics for the extinctiometer are located about 18 inches above the floor in the center of the chamber. Both the FSSP and the extinctiometer are located at approximately the same height. The transmitting and receiving optics for the extinctiometer are located outside of the chamber and light is coupled into and out of the Herriott cell via a transmitting and a receiving fiber. Kapton patch heaters have been installed on the back of each mirror to prevent water from condensing on the mirrors.
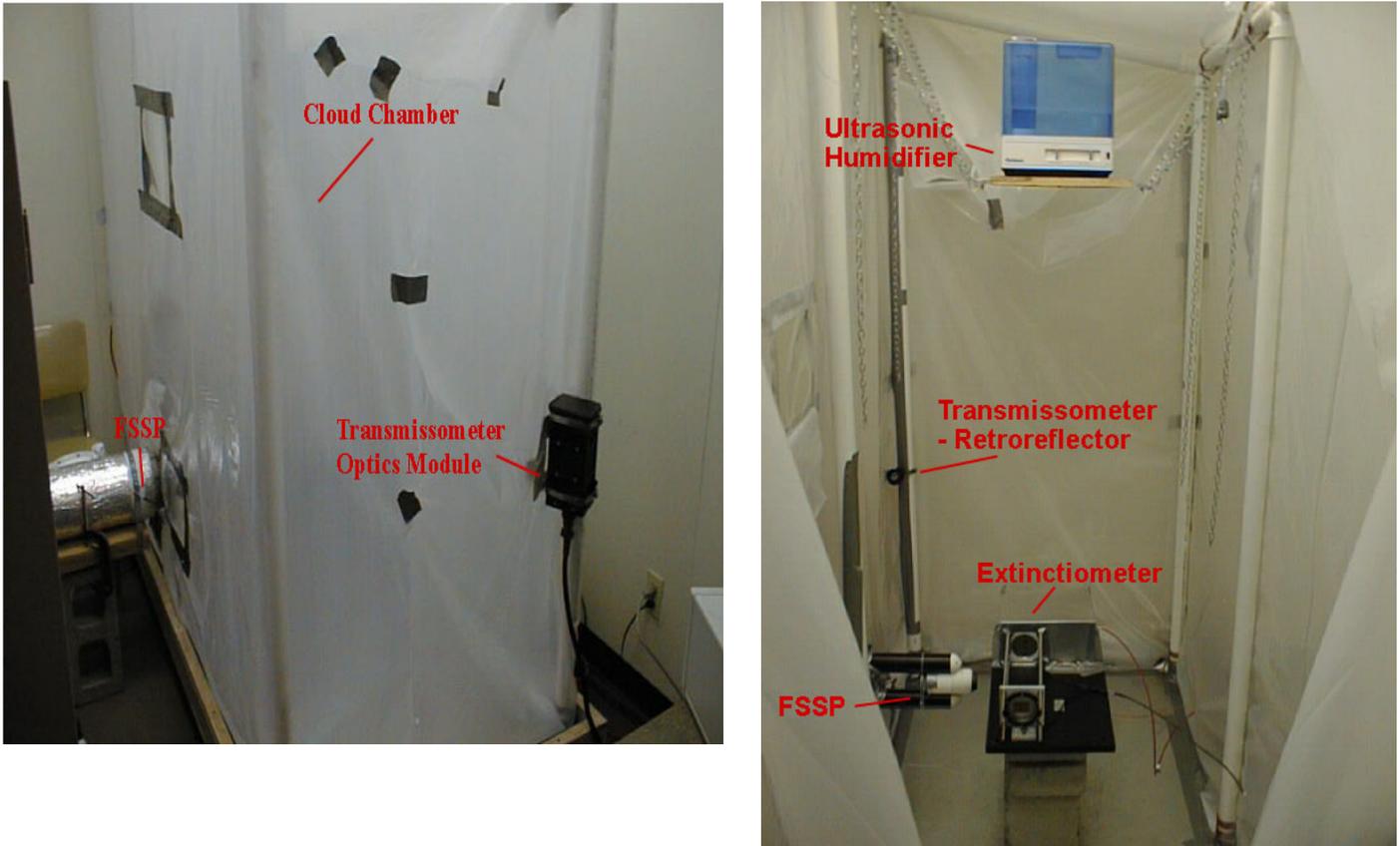
Figure 31. **a)** Cloud chamber constructed to compare extinctiometer, FSSP, and Russian Transmissometer and **b)** inside view.

The transmissometer operates on the same principle as the extinctiometer and is described by Beer's law **(Section 2.1, equation (3))**. The transmissometer utilizes an optical source and a retroreflector set at a fixed spacing to determine the optical path length. Cloud drops intersect the light beam and attenuate the signal received by the photodetector. The transmissometer uses an LED with a peak wavelength of 0.95μm as a light source and a silicon photodetector. A reference detector is used to cancel out source fluctuations. The initial location of the retroreflector in the cloud chamber can be seen in **Figure 31b.** In the pictured configuration, the separation of the optical module and retroreflector is approximately 1.97 m, giving a total path length of 3.94 m for the transmissometer.

Theoretical Calculation of Extinction Coefficient (β_λ,)

In the case of the extinctiometer, β_λ is calculated by rearranging equation (3).

$$\beta_\lambda = -ln\left(I/I_0\right)X^{-1} \qquad (12)$$

In the real-time software, this expression is evaluated using the instantaneous and background reference detector signal in the ratio to normalize out source fluctuations.

$$\beta_i = -ln\left[\left(\frac{signal\_i}{reference\_signal}\right)\left(\frac{signal\_i_{BKG}}{reference\_signal_{BKG}}\right)^{-1}\right]X^{-1}$$

$$(13)$$

In equation (6), i=1,2,3,...9 corresponds to each extinctiometer channel (Table 1), $signal\_i$ and $reference\_signal$ are the instantaneous signals for each channel and the reference detector (Table 4), and $signal\_i_{BKG}$ and $reference\_signal_{BKG}$ are the values for each channel recorded during a background (cloaking cycle). X is the total path length.

In the case of the FSSP, the extinction coefficient, β_λ, can be calculated based on the measured drop size distribution and the drop concentration (Liou 1980).

$$\beta_\lambda = \int_{r1}^{r2} \sigma_e(r)\frac{dn(r)}{dr}dr$$

$$(14)$$

where $\sigma_e(r)$ is the size dependent extinction cross section and $dn(r)/dr$ is the drop size distribution. The extinction cross section, $\sigma_e(r)$, is calculated by

$$\sigma_e(r) = Q_e \pi r^2$$

$$(15)$$

where Q_e is the extinction efficiency, calculated from Mie theory, and r is the particle radius. Q_e is dependent on size parameter, $x=2\pi r/\lambda$, and the refractive index of the drop and surrounding media. At wavelengths in the visible region, Q_e asymptotically approaches a value of 2 as x increases. **Figure 32** (top) is a plot of x versus Q_e for water, using a constant index of refraction equal to *1.33 + 0i*. While the index of refraction of water is wavelength dependent, the values of the real and imaginary parts are relatively constant over the extinctiometer wavelength range (Irvine and Pollack, 1968). At 2.13 μm, the imaginary part increases to 3×10^{-4}, and absorption may start to have an effect. However, the effects of absorption have been neglected for these calculations. **Figure 32** (bottom) is a plot of drop diameter, d, versus Q_e at three extinctiometer wavelengths.

For drop sizes measured at discrete size bins, the integral in (14) can be replaced by a sum

$$\beta_\lambda = \sum_{i=1}^{15} \sigma_i n_i$$

$$(16)$$

where n_i is the concentration in a FSSP size bin in number/cm^3, σ_i is the extinction cross section calculated for each size bin in cm^2, and the sum is taken over the fifteen size bins.

2.4.1.2   Results and Discussion of Cloud Chamber Data

The agreement between the instruments was a sensitive function of the orientation of the instruments in the cloud chamber. In the first configuration, the instruments are positioned as shown in **Figure 31b**. The transmissometer was pointed diagonally across the chamber and the extinctiometer was oriented with the optical axis parallel to the long side of the chamber. The FSSP was inserted into the side of the chamber at approximately the same height as the extinctiometer and with the sample tube near the center of the extinctiometer sample volume.

In order to move water drops through the FSSP sample volume it was necessary to use a small fan to aspirate the instrument. The fan used to aspirate the FSSP provided a flow rate of only 1.8 m/s through the FSSP sample volume. Operating the FSSP below 10 m/s will result in errors when calculating the drop concentration (Particle Measuring Systems 1977, Korolev 1999). An attempt was made to use an axial blower to increase the velocity through the FSSP, but the higher flow rate adversely affected the distribution of cloud drops in the chamber. For this reason, the FSSP was aspirated at a lower velocity. Due to low velocity through the FSSP sample volume, a scale factor has been applied to the extinction coefficient calculated using the FSSP data.

Figure 33a is a plot of the extinction coefficient measured by the extinctiometer, FSSP, and transmissometer. To calculate the FSSP extinction coefficient, an equivalent wavelength of 950 nm was used. The plot shows good qualitative agreement between the FSSP and both channels of the extinctiometer.   The transmissometer reports an extinction coefficient consistently higher than the extinctiometer. The difference in the measurement is most likely due to an inhomogeneous distribution of drops within the chamber. In order to produce a cloud within the chamber, the humidifier was turned on and the chamber was sealed. After about 75 minutes, the production of drops in the chamber reached an equilibrium with the loss of drops to the chamber walls and leaks out of the chamber. The value of β_λ measured by the extinctiometer rapidly increased to approximately 350 km^{-1}. At values much higher than 350 km^{-1} all of the light from the extinctiometer is consumed and the extinction measurement saturates. At this time the humidifier mist setting was turned to low and the extinction caused by drops in the chamber decreases to a steady state value of about 50 to 100 km^{-1}. At 120 minutes into the experiment, the humidifier was turned off and the value of β_λ gradually drops to zero.

A Helium Neon (HeNe) laser was used to visually examine the distribution of drops within the chamber. The laser was directed through a clear plastic window in the chamber and areas of high drop concentration were easily identified with the human eye. This technique showed that the distribution of water drops within

the chamber was very transient and that the transmissometer, FSSP and extinctiometer were not sampling the same sections of cloud within the chamber.

Figure 33b is a plot of the drop size distribution in the chamber over time. A histogram of drop size versus number is averaged for one minute and plotted every ten minutes throughout the experiment. In the plots shown, the minimum size bin is 3µm and the maximum size bin is 31µm. There are a total of 15 bins, each 2µm wide. At 85 minutes into the experiment, the drop size distribution has a peak at about 15µm. This time corresponds to the maximum extinction coefficient, before the humidifier was turned down. From approximately 95 minutes into the experiment until the humidifier is turned off, the mean drop diameter is approximately 8µm. The extinction coefficient is relatively constant throughout this same time period. Based on the plots in **Figure 9a**, the value of β_λ measured by the extinctiometer on both the 0.95µm and 2.13µm channels should be within approximately 5% of the theoretical value of the extinction coefficient at these wavelengths and a drop size of 8µm.

In an effort to make the cloud within the chamber more homogeneous throughout, a fan was used to circulate the drops within the chamber. The transmissometer orientation remained the same while the extinctiometer was rotated 90 degrees to facilitate circulation of the drops through the extinctiometer. **Figure 34a** is a plot of the extinction coefficients from all three instruments. In this configuration, the extinctiometer is reading higher than both the FSSP and the transmissometer. The data between the three instruments are in good qualitative agreement with the value of β_λ gradually decreasing over time. **Figure 34b** shows the drop size distribution over time. In this case the mean drop diameter is approximately 10µm throughout the experiment. The extinction coefficients are also correspondingly higher than those plotted in **Figure 33a**. Based on the curves in **Figure 9a**, the measured extinction coefficient should be within 7% of the theoretical value. Again, the HeNe laser was used to determine the distribution of cloud within the chamber. The results were similar to the previous case with small volumes of cloud drifting through the sample volumes of each instrument.

The location of the transmissometer was changed in an attempt to better match the sample volumes of the transmissometer and the extinctiometer. The transmissometer was set up with the beam pointing across the shorter side of the cloud chamber, parallel to the optical path of the extinctiometer. The separation of the optical module and retroreflector was reduced to 0.98 m for a total path length of 1.96 m. The tranmissometer beam was at approximately the same height as the extinctiometer and located within 12 inches of the sample volume of the extinctiometer. The circulating fan was not operating inside the cloud chamber during this run.

Figure 35a shows that the agreement between the extinctiometer and transmissometer improved after repositioning the instruments. Excluding the large spike from the FSSP measurement, all three instruments are in fairly good quantitative agreement. The drop size distributions are plotted in **Figure 35b** and are very similar to those in **Figure 33b**, with a mean diameter of

approximately 8μm. The HeNe laser still showed variations within the chamber, however, relocating the transmissometer may have improved the chance for the extinctiometer and the transmissometer to sample the same volume of air.

The experiment shows that the prototype Herriott cell based extinctiometer has fairly good qualitative and quantitative agreement with the Russian transmissometer. Comparison of the measurements was limited by the inability to produce a homogeneous distribution of drops within the cloud chamber, as well as insufficient airflow through the FSSP. Korolev et al. (1999) have shown very good agreement between the transmissometer and the extinction coefficient calculated from FSSP data in real clouds. The FSSP was operating within an acceptable velocity range during these flights.

The results from the cloud chamber tests were useful in proving the feasibility of using a Herriott cell based instrument to measure extinction coefficients. The comparison between instruments was relatively good given the circumstances, and the experimental results compare well with the theoretically predicted values of extinction coefficient. The decision to proceed with final instrument design was based on the results from these successful laboratory tests.

2.4.2 Wet Wind Tunnel

Tests of the sample head were conducted in a wet wind tunnel to evaluate the aerodynamic stability of the sample head and the performance of the wetless apertures and cloak actuation in flight-like conditions. The sample head was tested in a wet wind tunnel at Particle Measuring Systems (PMS) in Boulder, CO. **Figure 36** is a photograph of the sample head mounted to a PMS canister in the PMS tunnel. The test section in the tunnel is circular with a diameter of approximately 0.76 m. The tunnel is capable of achieving velocities up to 100 m/s. Water is injected into the tunnel with two sets of nozzles located upstream of the test section. Since the internal instrument components were not completed at this time, the test was performed with the optics modules and electronics located outside the tunnel. The transmit and receive fibers were connected to the sample head and passed into the tunnel through the support for the PMS canister (Engineering Prototype #1, Table 7).

The tunnel was not instrumented to measure liquid water content (LWC), drop concentration or drop size distribution. Quantitative comparisons between the extinctiometer readings and the actual extinction coefficient were not possible in the absence of other instruments for comparison. The LWC was estimated by measuring the airflow through the test section and the flow rate of the water injected by the nozzles. The maximum LWC in the tunnel is approximately 0.58 g/m^3 based on the ratio of the flow rates of water to air.
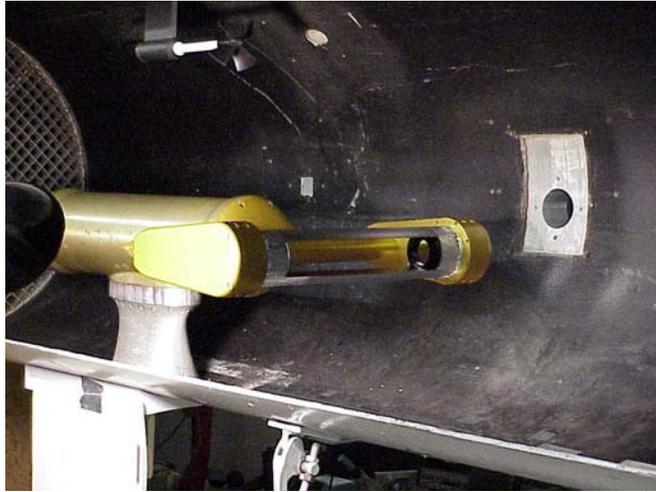
Figure 36. Extinctiometer sample head in wet wind tunnel during first round of tests.

The aerodynamic stability for the instrument was also evaluated in the tunnel at velocities up to 100 m/s. The extinctiometer was installed in the tunnel and the velocity was gradually ramped to 100 m/s. The instrument remained relatively stable without any strange oscillations or vibrations at 100 m/s.

While the tests did not produce quantitative results, they did give a qualitative indication of how the apertures were performing. A video camera was focused on one of the mirrors and apertures and used to observe the flow of water drops past the apertures. While running near the maximum LWC values for the tunnel, drops were occasionally seen to be dragged from the back of the aperture forward onto the mirror, against the direction of free stream flow. This was evidence of recirculating flow in the apertures themselves, over the mirror surfaces.
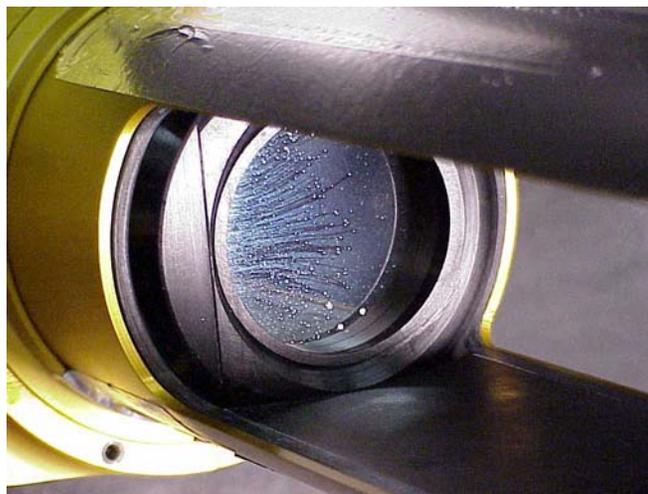

Figure 37. Close up of contaminated mirror in wind tunnel.

Figure 37 is a close up view of one of the contaminated mirrors, showing the streaks left by the drops being dragged across the mirrors. In this case airflow is from right to left and the drops are dragged in a direction opposing the flow. Drops would accumulate on the rear step shown in the photo. They would then become entrained in the recirculating flow over the aperture and be dragged onto the mirror surface. If the drops simply evaporated, there would be no streaks left behind. The streaks may be due to the high mineral content of the water injected into the tunnel. Water drops in the atmosphere will have much lower mineral content than those encountered in the tunnel. The result of the contamination on the mirrors was approximately a 30% reduction in the baseline extinction signal without any drops blocking the beam. During actual flight, a new background could be taken to remove this baseline extinction signal, but additional contamination could eventually block all of the incident light beam.

Based on the results from these tests, "turbulence fences" (i.e., flow straighteners) were added to the instrument in hopes of improving the contamination problem (engineering prototype #2, Table 7). The fences are simply 9" diameter Aluminum plates attached to the outer cylinder that rotate with the cloak when it is closed. The addition of the turbulence fences more closely resembles the geometry that was modeled using Star-CD. **Figure 38** shows the sample head installed in the PMS tunnel with the new turbulence fences. The contamination problem seemed to improve greatly with the addition of the turbulence fences. There was no detectable contamination on the mirrors when the tunnel was operating near its highest LWC values. **Figure 39** is a measure of the repeatability of the instrument in the wet wind tunnel. Two detectors are operating during this test. Channel 6 and Channel 9 show the extinction for these spectral channels. The spray nozzles are turned on and off three times and the extinction coefficient measures approximately 50 to 70 km-1 for each cycle.

The actuation of the cloak was also evaluated in the wind tunnel. The CO_2 system regulator pressure was set to 100 psi to power the double acting cylinder. The cloak operated smoothly with the tunnel velocity at 100 m/s. The spray nozzles where set at maximum LWC and the cloak was cycled. The cloak reliably blocked the flow of drops into the sample volume when it was closed. However, opening the cloak would occasionally cause drops accumulating on top of the inner cylinder to be "washed" into the sample volume when the cloak was opened. Some of these drops would eventually land on one of the mirrors. Flight testing was necessary to determine if this problem would be replicated while flying through natural clouds in the atmosphere.

2.4.3 Extinctiometer Test Flight #1 (032400) on Learjet

Installation of Instruments on Learjet

Modifications were made to the Learjet leased by SPEC to accommodate the mounting of the extinctiometer and the Russian transmissometer. A transmissometer was previously installed on the Canadian Twin Otter and measurements are described by Korolev et al. (1999). Two additional mount

points and pylons have been installed on the fuselage of the Learjet to house additional PMS style probes. The new probe mount points and pylons were certified by the FAA and flight tested.
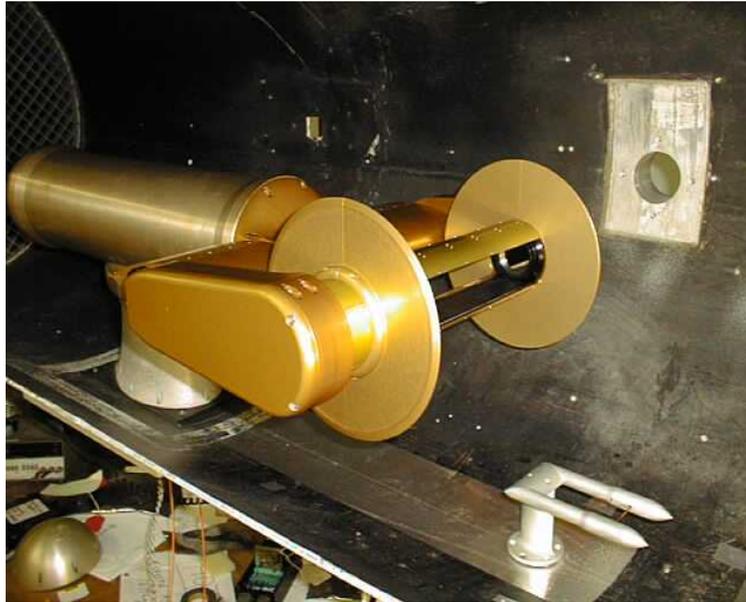

Figure 38. Extinctiometer sample head in wet wind tunnel during second round of tests with turbulence fences installed.
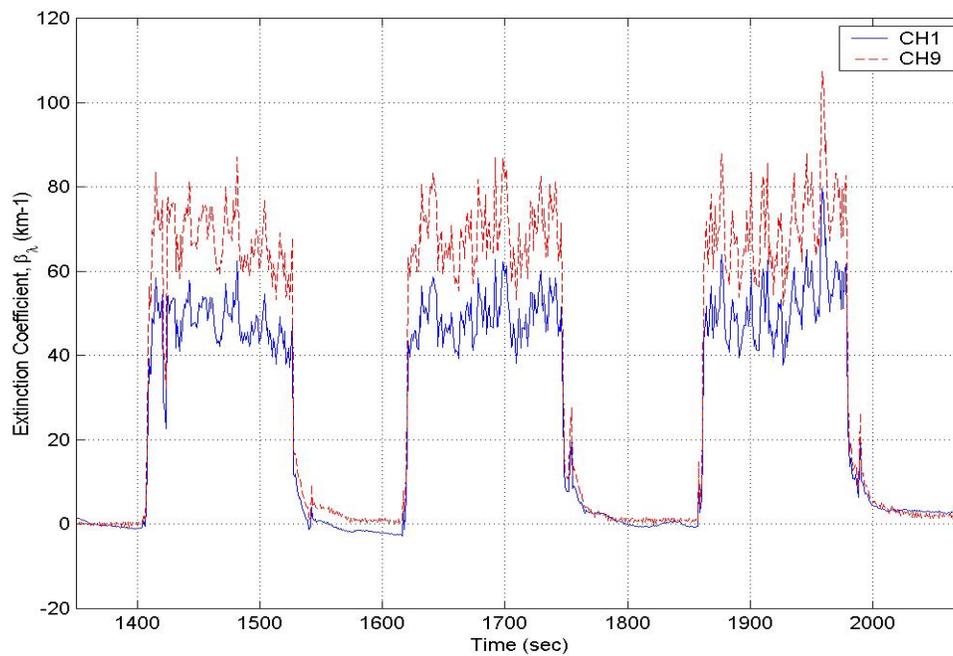

Figure 39. Repeatability of Extinctiometer in PMS wind tunnel. Note that the signal returns to the baseline after spray is turned off, indicating that the mirrors are free from contamination.

The transmissometer was mounted with the source and detector module inside the aircraft and the retroreflector installed on the wing tip. The light beam was directed through the aircraft window to the retroreflector mounted on the starboard wing tip-tank . The beam is then reflected back to the detector inside the aircraft. The round trip optical path length for the transmissometer is approximately 8 m, fairly close to the folded path of the extinctiometer. **Figure 40** is a photograph showing the location of the tranmissometer beam path and the extinctiometer on the Learjet. Data from the transmissometer will be compared to measurements taken with the extinctiometer.
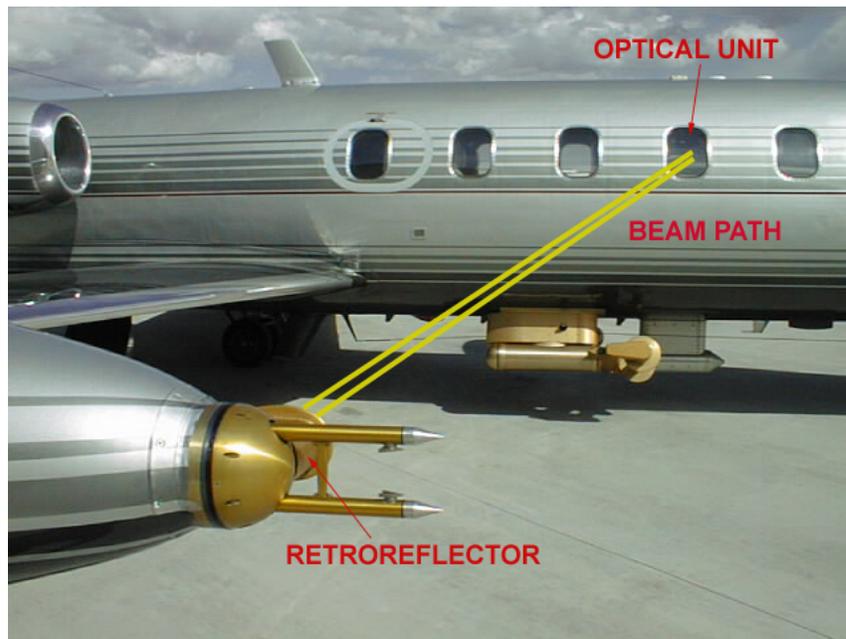

Figure 40. Location of transmissometer components and beam path on Learjet. The extinctiometer is also shown mounted on a pylon under the fuselage.

An aerodynamic shroud has been designed to house the retroreflector on the wingtip. **Figure 41** is a photograph of the shroud and retroreflector mounted behind the dome for the PMS 2-D probe. The retroreflector is slightly recessed from airflow behind a "wetless" aperture to keep the optic free from contamination. Coarse angular adjustments are located inside the shroud to roughly point the retroreflector in the correct direction. The optical unit mounts on a custom designed alignment stage on the data rack inside the aircraft. The unit points out a starboard window and can be adjusted for tip and tilt. The transmission loss through the aircraft window attenuates the beam slightly, but the attenuation is a constant and normalized out of the extinction measurement as part of the background signal. A coarse alignment is performed by adjusting the optical unit until a return signal is present on the detector. The tip and tilt adjustments are then used to maximize the signal.

Figure 41. Side and head on views of transmissometer retroreflector shroud.

Excluding laboratory testing, this flight was the first fully integrated system test of the completed extinctiometer, including the completed sample head, internal components, electronics and real-time software (engineering prototype #3, Table 7). The extinctiometer was operated with three of the nine channels functioning for each of the research flights. The channels used were Channel 6 (950 nm), Channel 8 (1640 nm) and Channel 9 (2130 nm). **Figure 42** is a photograph of the extinctiometer with all of the subsystems fully integrated.
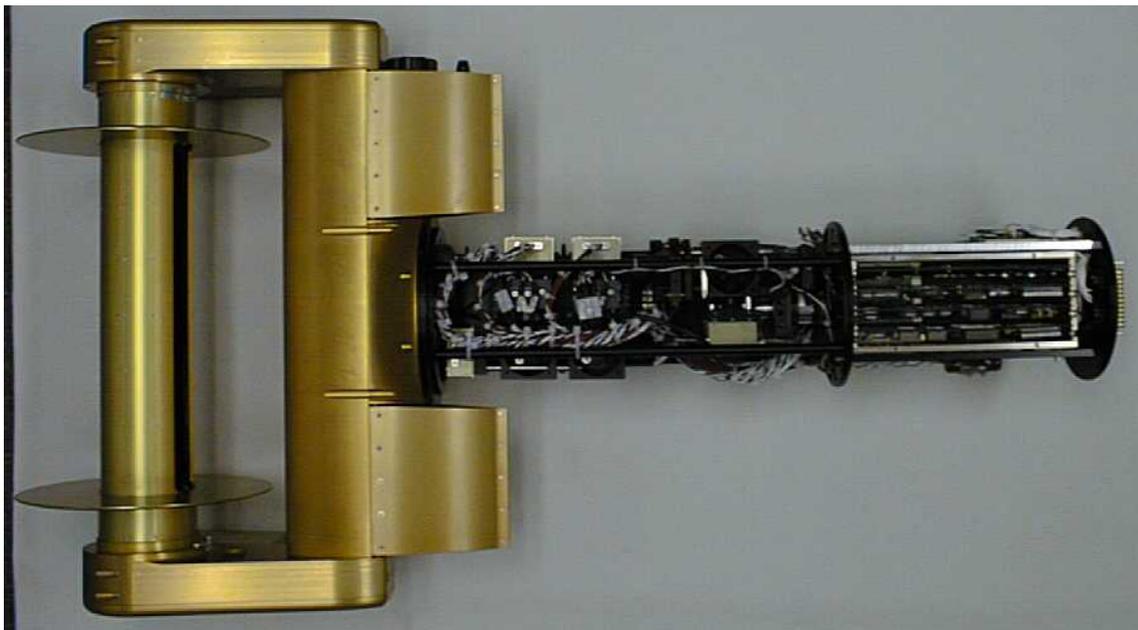

Figure 42. Extinctiometer with all subsystems fully integrated and turbulence fences installed.

The extinctiometer is mounted in the newly installed pylon under the fuselage on the starboard side of the aircraft. **Figure 43** is a photograph of the extinctiometer mounted on the aircraft. The top view in this photograph also shows the SPEC Cloud Particle Imager (CPI) and SPP-100 under the fuselage. The extinctiometer mounts by simply sliding it into the PMS can and tightening

74

down the eight screws on the transition. The connector mates automatically as the instrument slides into the can. The real time software runs on a laptop PC (**Figure 30**) and is controlled by an operator sitting in the aircraft.

The SPEC research aircraft is instrumented to make cloud microphysical measurements. State parameters such as temperature and pressure are measured and recorded by a Science Engineering and Associates (SEA) data system. A King hotwire probe (King et al. 1978) measures LWC and a Nevzorov hotwire probe measures total water content (TWC) and LWC (Korolev et al. 1998). The TWC measurement is based on the same principles as a hotwire, using a heated cone instead of a wound wire. Particle concentration and size are measured using a PMS 2D-C, an FSSP (Knollenberg 1981) and the NCAR SPP-100. The SPP-100 is an FSSP with faster electronics (zero dead time). The SPEC CPI measures concentration and size and provides high resolution images of cloud particles (Lawson et al. 2000). A Rosemount icing probe detects the presence of super cooled liquid water (Baumgardner and Rodi 1989). In addition to these instruments, the Russian transmissometer has been installed, as described above, for comparisons with the extinctiometer.

Results from 032400 flight

The first test flight of the airborne extinctiometer was conducted on March 24, 2000 over North-Central Colorado and South-Central Wyoming. The aircraft took off from Jefferson County Airport outside of Broomfield, Colorado and gradually climbed to 18,000 feet. The instrument was operated in clear air for a substantial period of time to allow the pilots to evaluate the effect of the instrument on aircraft performance. The cloak was periodically actuated to confirm its operation at aircraft speeds. The pilots reported no effect on aircraft performance from the installation of the extinctiometer.

Figure 44 is a plot of the extinction coefficient for three extinctiometer channels and the transmissometer while in clear air. The time period shown is approximately four minutes after the aircraft had reached a constant altitude of 18,000 feet. This plot gives an indication of the baseline stability of the extinctiometer during constant altitude flight. The stability is approximately +/- 2 to 4 km^{-1} for the three channels shown. The stability of the Russian Transmissometer during this period is about +/- 3 km^{-1} during level flight.

An earlier test flight of the transmissometer had shown that the stability of the transmissometer is highly dependent on whether or not the aircraft is maneuvering. The transmissometer alignment was performed on the ground and then optimized during level flight. When the aircraft performs a turn, the deflection of the wingtip was enough to affect the baseline extinction measurement for the transmissometer as much as 10 - 70 km^{-1} depending on the g-forces experienced during the turn. For this reason, the data from the transmissometer is only useful while the aircraft is in level flight. Flying through turbulence during level flight, the wing tip deflection is averaged out and the data is useful, although the noise in the measurement may be increased slightly. This

flight limitation on the transmissometer could possibly be overcome by mounting both the optical unit and the retroreflector along the fuselage of the aircraft. A drawback of this mounting scheme is that it would require substantial modifications to the Learjet.

The extinctiometer exhibited very good stability while the aircraft was maneuvered and flown through turbulence. The primary limitation in the sensitivity of the extinctiometer is thermal drift, discussed in following sections. **Figure 45** is a plot of the extinction coefficient measured by the extinctiometer and transmissometer while penetrating a line of small cumulus congestus clouds. **Figure 46** is a photograph of the line of cumulus clouds. There is excellent agreement between these two instruments and β_λ as high as 250 km^{-1} were measured. **Figure 47** is scatter plot showing the correlation between the extinctiometer and transmissometer measurements. The correlation coefficient for the plot is 0.91. It is likely that the outlying points may be a result of the turbulent g-forces encountered in the clouds, moving the transmissometer beam off of the retroreflector. **Figure 48** is a plot of β_λ calculated from the FSSP concentration and size distribution using equation (8) at the three wavelengths corresponding to extinctiometer channels 6, 8 and 9. Qualitatively the data track very well, however, the value calculated by the FSSP is approximately a factor of 5-6 times lower than the extinction coefficients measured with the transmissometer and extinctiometer.

Figure 46. Cumulus congestus line penetrated on March 24 2000.

Figure 49 is a plot of the King LWC and the LWC calculated from the FSSP concentration and size spectra. **Figure 50** is a scatter plot of FSSP LWC versus King LWC. By fitting a line to the data, this plot shows that the FSSP LWC is approximately 5.4 times lower than the LWC measured by the King probe. The correlation coefficient for the scatter plot is 0.923. Using a scale factor of 5.4, the scaled FSSP LWC is plotted in **Figure 49**. Scaling the FSSP LWC to match the King provides better agreement between the measurements, however the scaled FSSP LWC still overestimates the measurements made by the King in some regions and underestimates the King LWC in other regions.

Figure 51 is a plot of the Channel 6 extinction coefficient (blue) and the extinction coefficient calculated by the FSSP (green) at 950 nm. The red trace in **Figure 51** is the FSSP based extinction with the scale factor of 5.4 applied. For values of β_{950} below about 100 km^{-1}, the scaled FSSP measurements agree fairly

well with Channel 6. For values of β_{950} greater than 100 km^{-1}, the scaled FSSP tracks the CH6 measurements well, but underestimates the values by thirty to forty percent. **Figure 52** is a scatter plot of the scaled FSSP extinction versus Channel 6. The correlation coefficient for the plot is 0.95.

Figure 53 is a plot of the Nevzorov total water and liquid water contents and the King LWC. The TWC indicates the presence of ice from approximately 2150 to 2250 seconds. After this time the LWC and TWC measurements are in close agreement, indicating that the cloud particles are mostly water drops. The LWC is fairly high through this cloud, peaking between 0.4 and 0.5 g/m^3. During flight, the domes on the wing tip probes experienced substantial riming, verifying high LWC values. **Figures 54** and **55** are CPI images corresponding to the periods near 2200 seconds and 2325 seconds in **Figure 53,** respectively. The CPI images support the Nevzorov readings, showing large (200 – 600µm) rimed ice crystals near 2200 seconds and showing the drop concentration increasing substantially at 2325 seconds. Large ice crystals are still present with the drops, however. Although the FSSP concentration and size spectra may be adversely affected by the presence of ice, the disagreement between the calculated extinction coefficients and the values measured by the extinction instruments disagree by about the same amount with or without ice dominating the TWC measurement.

This first test flight was successful in demonstrating operation of the extinctiometer in flight through mixed phase clouds with fairly high extinction coefficients. The wetless apertures worked well, keeping the mirrors free from contamination in relatively high particle concentrations (~200 cm^{-3}, diameter 3-45µm) of super cooled liquid water. The alignment of the instrument was insensitive to vibration and g-loading. The baseline drift was slightly higher than we would have hoped for, but the measurements are very useful due to the high values of extinction. The data system operated reliably, recording and displaying data throughout the flight. The cloaking system failed to actuate near the end of the flight due to a leak in the CO_2 regulator. Unfortunately, this component could not be replaced before the end of the flight program, due to a long manufacturer's lead-time. The cloak was locked in the open position for the rest of the flight program and could not undergo further evaluation during flight.

2.4.4 Extinctiometer Test Flight # 2 (032700) on Learjet

The research flight on March 27, 2000 was to investigate cirrus clouds. The instrument was operated in the same configuration as the previous flight (engineering prototype #3). Unfortunately, shortly after take off the extinctiometer experienced a step change in baseline signal which decreased the incident light levels by approximately 50 %. Upon inspecting the instrument after landing, it was found that the 200µm core transmit fiber had become loose in the fiber coupling barrel. The fibers are potted into clearance holes drilled into the barrel using an RTV potting compound. The fibers make a 90 degree turn after exiting the barrel, at the minimum specified bend radius for the fiber. This assembly is fairly complex to manufacture, requiring a microscope to position the ends of the fibers in the same plane. The RTV did not adhere well to the fiber,

resulting in an assembly in which it was possible to translate the fibers a small amount. The bond was eventually broken by the residual stress caused by the bent fiber trying to straighten itself out.

The fibers were repotted into the barrel using a high strength Eccobond epoxy and the mechanical design was altered to provide more surface area for bonding on both the fibers and the barrel. The instrument was realigned and reassembled. The resulting bond was much more rigid using the epoxy compared to the RTV. Movement of the fibers was not evident as the fibers were manually pushed and pulled along their axis.

2.4.5 Environmental Chamber Test #1

Temperature testing was performed at this time to investigate the temperature dependence discovered during test flight #1. The tests were conducted at the NCAR environmental chamber. The completed instrument was placed in a PMS canister and then placed in the chamber. A test cable was used to run signals from the back of the canister to the data system located outside the chamber. The temperature was stepped from $25°$ C to $-45°$ C in intervals of $10°$ C to measure the effects of temperature induced changes in the optical alignment. The shifts in alignment result in drift of the baseline extinction signal.

Figure 56a/b is a plot showing oven temperature and Channel 6 extinction coefficient over time. In this experiment the chamber setpoint is changed every twenty-five minutes. Because Channel 6 is normalized by the reference detector, which operates over the same spectral range as Channel 6 (center wavelength =950 nm), the changes in the extinction signal are primarily temperature induced.

The maximum deviation in the Channel 6 extinction coefficient is approximately 8 km^{-1} peak to peak. As the chamber setpoint is changed, the ambient temperature in the chamber reaches the setpoint on the order of a few minutes. A fan circulates the air in the chamber, providing minimal convective heat transfer to the instrument. Due to the large thermal mass of the instrument, there is a very long thermal lag between the temperature change of the chamber and the temperature change of the instrument.

Figure 56b shows a step change in the signal corresponding to the chamber temperature change at each step. The signal then starts to slowly relax and move toward an equilibrium value. The equilibrium value is not reached due to the inadequate time spent at each temperature point (twenty-five minutes). Repeating most chamber temperature setpoints twice, one cooling down and the other heating up, the equilibrium values for the extinction coefficient do not appear to be the same. Based on this experiment, it was determined that the sensitivity of the instrument to temperature changes is the limiting factor on the resolution of the extinction measurement.
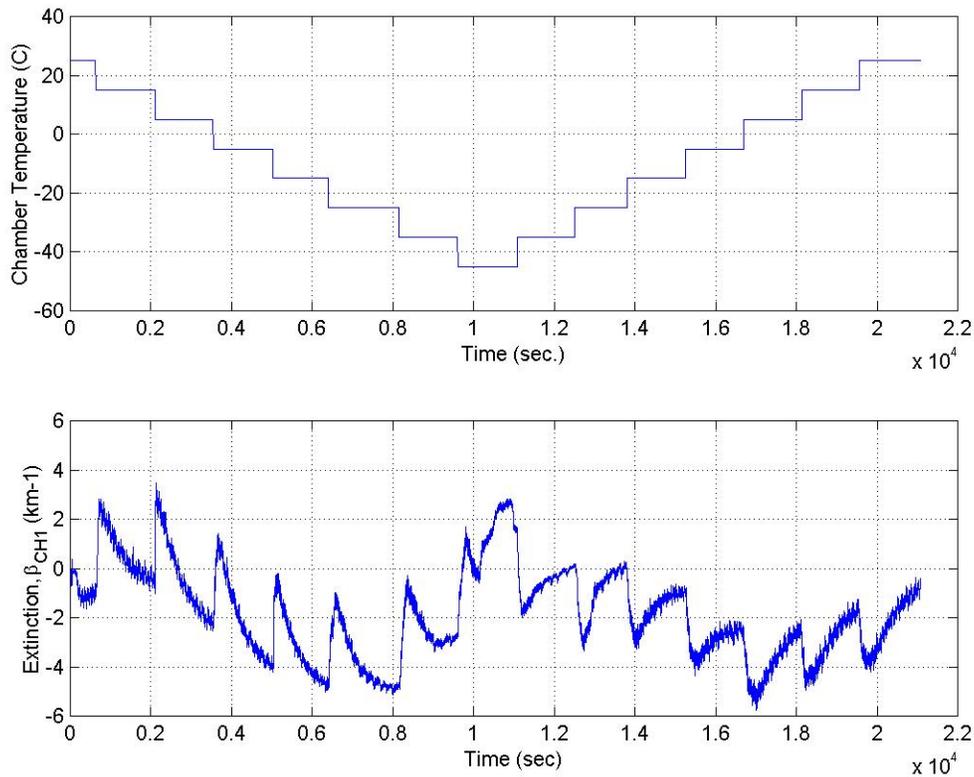
Figure 56. a) Chamber temperature and **b)** CH6 extinction showing temperature induced drift.

Figure 57 is a plot of the extinctiometer running in the laboratory with the cloak opened and closed. At a stable temperature, the difference in the cloak open and closed positions indicates the response of the instrument to aerosols suspended in the room. The extinctiometer responds to changes in extinction coefficient on the order of +/- 0.1 km^{-1}. If the temperature stability of the instrument were improved during flight, it is possible that the instrument may be sensitive enough to measure aerosol extinction.

During the environmental chamber testing, the extinctiometer heaters were not running, but the temperatures for each heat zone were monitored and recorded. The changes in the extinction signal are well correlated with changes in the outer cylinder temperature, mirror temperature, inner cylinder temperature and aperture temperature. The temperature of the internal components is also recorded and does not seem to be well correlated with the change in signal. This would indicate the temperature sensitivity lies in the sample head and not in the internal components such as the transmitting and receiving optics modules.

In addition to evaluating the temperature sensitivity of the optical alignment, the testing showed that a spectral drift existed in the lamp output as a function of ambient temperature. This drift causes the baseline extinction signal for all
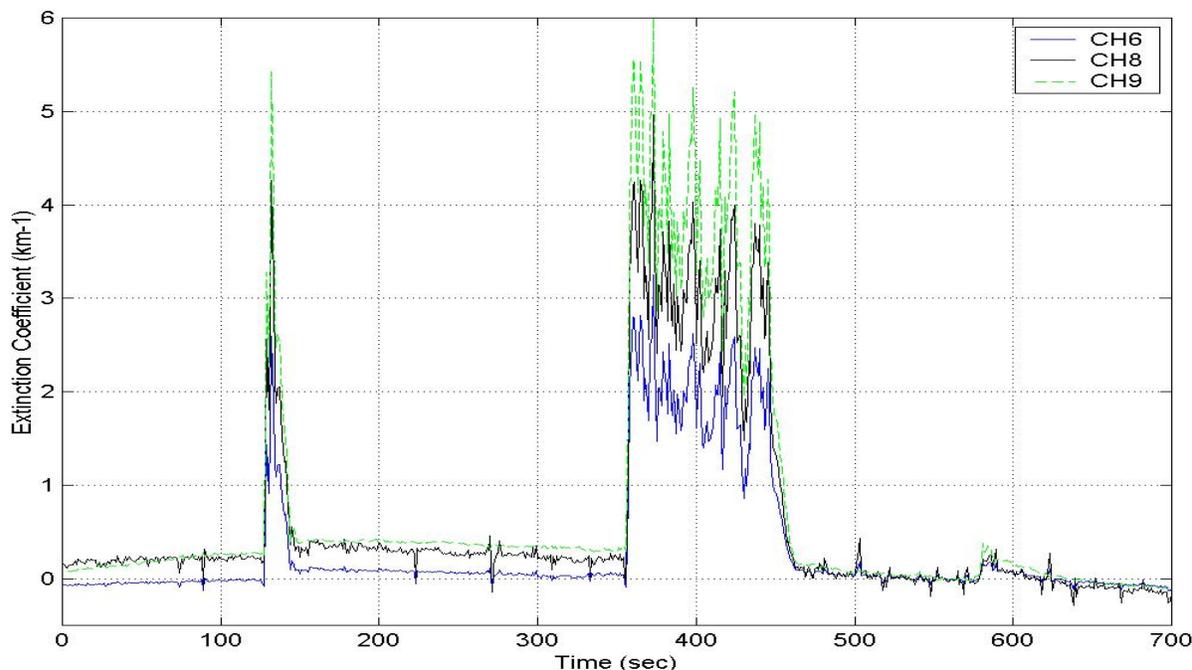
Figure 57. Instrument stability in laboratory with cloak opened and closed.

channels other than Channel 6 to drift as the temperature surrounding the lamp changes. A temperature sensor was installed near the QTH lamp to record the ambient temperature near the lamp. Using data in clear air, the difference in signal between Channel 9 and Channel 6 and Channel 8 and Channel 6 versus lamp temperature can be used to correct the extinction measurement for spectral drift in the lamp.

2.4.6 Extinctiometer Test Flight #3 (041200) on Learjet

The third research flight was conducted on April 12, 2000 over the ARM / CART site outside of Ponca City, Oklahoma. The instrument configuration is engineering prototype #4 (Table 7), the same as the previous flight, except the fibers have been re-potted and the lamp temperature was recorded. **Figure 58** is a plot of the extinction coefficients measured by the extinctiometer and the transmissometer. The baseline drift for the extinctiometer is similar to the first flight. The plots for Channel 8 and Channel 9 in **Figure 58** have a compensation factor applied. The compensation algorithm was developed by plotting the lamp temperature versus Channel 9 minus Channel 6 in clear air. In this case, if it is assumed that the thermal induced alignment drift is wavelength independent, the difference between the channels should be primarily caused by spectral drift of the lamp. Since the Herriott cell uses reflective optics (focal length independent of wavelength), the assumption is probably valid. A curve is fit to the difference of Channel 9 minus Channel 6, with lamp temperature as the independent variable. In post processing, this difference in signal is evaluated based on lamp temperature, and this factor is then subtracted from the Channel 9 extinction measurement. The same procedure is followed for Channel 8.

Figure 58 shows that the transmissometer and extinctiometer have periods of relatively good agreement. **Figure 59** is a scatter plot of the tranmissometer and CH6 data.   The correlation coefficient for the scatter plot is 0.86. Only a short section of data is presented for comparison. The aircraft is maneuvering and changing altitude to stay in cloud during this thirty-minute flight leg, so the usefulness of the transmissometer data is limited.

The data were collected in mixed phase stratus clouds, with extinction coefficients reaching a maximum between 40 and 45 km^{-1}. As expected, these values are lower than the extinction coefficients measured in Cu during the first test flight. Russian transmissometer data for cold stratus clouds (analyzed in Phase I), shows average extinction coefficients of approximately 25 km^{-1} in stratus with maximum values between 40 and 60 km^{-1} (Phase I final report reference). **Figure 60** is a plot of the King LWC, showing peak values near 0.2 g/m^3. The LWC values are much lower than those on the March 24, 2000 flight, resulting in correspondingly lower extinction coefficients.   The FSSP and Nevzorov probes failed during this flight, so extinction coefficients can not be calculated from the FSSP data.

2.4.7 Herriott Cell Thermal Stability

The results of three test flights and the temperature test prompted an investigation into the thermal stability of the optical bench housing the Herriott cell. The fiber-to-Herriott cell coupling barrel and associated adjustments were removed from the sample head. A HeNe laser was injected into the Herriott cell at the same injection angles as the beam from the QTH lamp. The output beam was coupled out of the cell and its location was marked on a target located three meters away form the Herriott cell entrance mirror. The Amalgon cylinder was thermally stressed using a heat gun and by cycling the inner cylinder temperature heater to relatively high temperatures. The maximum deviation of the output beam from its initial position on the target was measured to be approximately 3 mm. In the plane of the mirror, this corresponds to translating the output beam across the fiber coupling lens by approximately 300 µm.

A ray tracing analysis of the output beam, coupling lens and 365µm receive fiber indicates that all of the light should be coupled into the fiber. The analysis shows that translating this beam by 300µm across the lens still results in coupling all the light into the receive fiber. The measured drift of the baseline signal far exceeds the amount of drift in signal explained by movement of the output beam. The alignment procedure for the Herriott cell was investigated as the next possible cause for the baseline drift in signal.

The first step in the alignment procedure for the Herriott cell involves setting the spacing between the transmit fiber and coupling lens to get a fairly collimated input beam. The next step is to adjust the angle and position of the fiber-to-Herriott cell coupling barrel to point the input beam at a fixed location on a target inserted into the Herriott cell. Correct alignment on the target injects the beam at the required angle and position to satisfy the reentrant condition. The position of the receive fiber is fixed with respect to the transmit fiber by the fiber-to-Herriott

cell coupling barrel described in **Section 2.3.1**. The position of the coupling lens with respect to the receive fiber is already set when the input beam is collimated, because the same lens is used for both fibers (**Figure 13**).

While this approach to coupling (described in **Section 2.3.1**) is spatially compact and efficient, it fixes two degrees of freedom in the alignment geometry. The angles between the two fibers are designed into the coupling barrel and are not adjustable. The holes in which the two fibers mount in the barrel are drilled to very tight tolerances and the angle between the holes is manufactured to a tight tolerance. The mechanical dimensions for the design were calculated based on ray tracing analysis and numerical simulation of the beam position within the Herriott cell. The beam positions could not be measured due to the very small available space. The second limitation in the alignment is that moving the coupling lens with respect to the fibers changes the collimation of the input beam and the focus of the output beam onto the receive fiber.

To determine if the optimization of the alignment was limited by the mechanically designed in parameters, the beam was coupled out of the far side of the Herriott cell in the laboratory. This was accomplished by drilling a hole in the mirror opposite the entrance mirror. The mirror was rotated to position the hole so the beam would exit on the 25th pass. The optical path length was shortened from 8.29 m to 7.9 m. Because the receive fiber was epoxied in place, a separate 365µm receive fiber and coupling lens were used to couple the output beam from the opposite side of the cell on the 25th pass and deliver it to the receiving optics. Laboratory optics mounts were used to position this fiber and lens. In this geometry, the baseline light levels on the detectors did not increase significantly compared to coupling the beam out of the input side. Thermally stressing the Amalgon cylinder resulted in a drift in baseline extinction signal on the same order as the previous coupling geometry. This would indicate that the mechanical parts were designed and manufactured correctly and the thermal drift was not caused by a limitation in the alignment or the designed in place mechanical constraints.

Visual inspection of the spots on the Herriott cell mirrors showed that some spots came fairly close to the aperture. As the beam was refocused through the cell, some spots on the mirrors were much larger than other spots and were extremely close to the aperture. By adjusting the collimation of the input beam it was observed that the focus of the beam inside the cell shifted, but the clearance between the spots and aperture never improved.

With the 365µm receive fiber set up to couple the beam out of the cell on the 25th pass as described above, the 200µm transmitting fiber was replaced with a 100µm fiber. An aspheric lens with a smaller numerical aperture was used to collimate the input beam into the cell. This arrangement resulted in an input beam that was much better collimated and smaller than the original beam, due to the 100µm fiber more closely resembling a point source. The smaller spot size resulted in more clearance between the spots and the edge of the aperture. Thermally stressing the inner Amalgon cylinder showed an improvement in baseline drift by approximately a factor of four on the Channel 6 extinction

coefficient. This indicates the primary cause for the drift was the beam slightly hitting the aperture or the coupling hole in the mirror. As the optical bench contracted or expanded with temperature, the amount of light hitting the fiber would change slightly as more or less of the beam was clipped by the aperture.

The next logical step would have been to go back to the original coupling geometry, with the beam exiting the cell on the 26th pass, and determine if the problem had improved by decreasing the transmit fiber size. The fiber-to-Herriott cell coupling barrel would have to be redesigned and manufactured for a 100µm transmit fiber and a 365µm receive fiber and stripped and cleaved custom fibers would have to be ordered. Due to limited aircraft time remaining and the long lead times associated with the manufacture and assembly of the parts, as well as the possibility that the new parts may not work, an alternative solution was necessary.

To make the instrument flight ready in a short time frame, with the coupling geometry that had been proven in the laboratory, a set of opto-mechanical adjustments identical to the input side of the optical bench were manufactured and installed. While the pathlength was shortened by one pass, this arrangement allowed all necessary degrees of freedom for alignment, as well as the possibility of using the new off-the-shelf fibers and new aspheric coupling and collimating lenses. To improve the sensitivity of the output beam to misalignment, a 400µm core receiving fiber was installed. The new configuration resulted in less light coupled into the system because the power coupled into the fiber is proportional to the area of the fiber. The gains on the detectors were increased to overcome this loss of signal. The signal to noise ratio on the detectors was still very high and far from being the limiting factor in the measurement.

2.4.8 Extinctiometer Test Flight #4 (042600) on Learjet

The fourth test flight was the final flight for the project. The instrument was configured as described in the previous section (engineering prototype #5, Table 7). The Nevzorov probe and the FSSP were repaired and were operating on this flight. The SPP-100 was also installed on the Learjet for this flight.

The Lear made a series of passes through a weak system of wave clouds that were located about 100 Km southwest of Denver at an altitude of approximately 24,000 feet. **Figure 61** shows a photograph of the system of wave clouds looking southwest from the cockpit of the Learjet. **Figure 62** is a plot of β_λ for CH6, CH8 and CH9 shortly after reaching constant altitude. In this figure, the measurements are primarily in clear air with the exception of a few thin clouds indicated by the spikes. Of interest in this plot is the significant increase in stability of the baseline extinction signals in clear air. The drift for channel 6 is about +/- 0.6 km^{-1}, and channels 8 and 9 drift about +/- 1.5-2 km^{-1}. This is a substantial improvement compared with the baseline drift of the signals plotted in **Figure 44**, improving the sensitivity in the extinction measurement by a factor of 2-3. Both plots are for flight legs at constant altitude and temperature. The design changes in the fiber coupling to and from the Herriott cell have resulted in

a significant increase in sensitivity of the airborne extinctiometer. Improving the spectral stability of the lamp (implementing temperature control), or further refining the compensation algorithm using a more complete data set, would probably further improve the drift for channels 8 and 9.

Figure 61. Photograph of wave cloud studied on 26 April 2000 by the SPEC Learjet.

Figure 63 is a plot of the extinction coefficients measured by the extinctiometer and transmissometer during one pass through a fairly thick wave cloud. Extinctiometer CH8 and CH9 have been compensated for lamp temperature drift. For the cloud pass between 1800 and 2150 seconds, there is good agreement between the two instruments. The baseline tranmissometer signal is slightly high at about 2150 seconds even though the aircraft is flying a constant heading and constant altitude. **Figure 64** is a scatter plot showing a correlation coefficient of 0.97 between the transmissometer and CH6. The improved correlation (compared with **Figure 47**) is likely due to both the increased stability of the extinctiometer and the lack of turbulence in the wave cloud. (Recall that the transmissometer gives erroneous readings in turbulent air due to the beam wandering off of the retroreflector.)

Figure 65 shows measurements from the data system as the Lear flew at FL240 (-26° C) on a northeast heading from the leading edge to the trailing edge of cloud. The liquid water traces in the center of the figure are the Nevzorov LWC (red) and total (condensed) water content (TWC - green), which includes both the liquid and solid phases. The traces show that some of the liquid is converted to ice, indicated by the TWC exceeding the LWC, as the particles proceed through the wave cloud (right to left on the figure). The 2D-C images, FSSP and 2D-C particle size distributions are at the point in time at the far left edge (downwind) of the LWC trace. **Figure 66** shows examples of CPI images

collected throughout the wave cloud. The leading edge was composed entirely of water drops and ice was not detected until the crystals reached about 200µm in size (due to threshold settings on the CPI).
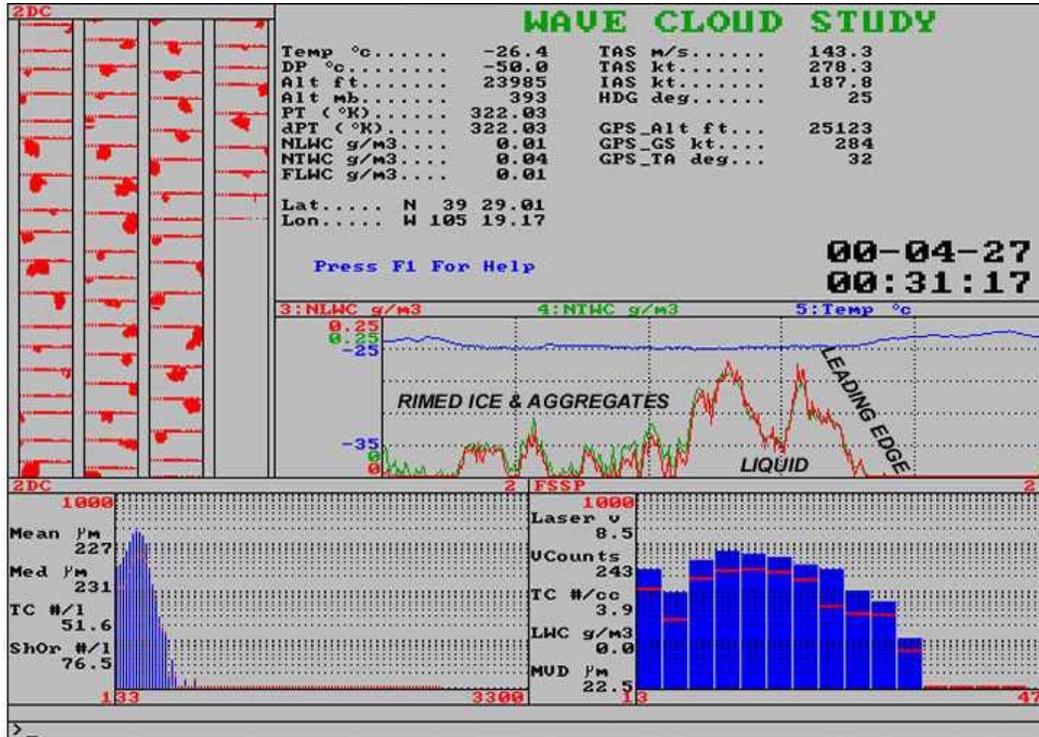

Figure 65. Screen showing various parameters collected by the SPEC Learjet in a wave cloud. The strip chart in the middle shows LWC (red) and total ice plus liquid water content (green) from the Nevzorov probe. Liquid is converted to ice proceeding downwind from the leading edge. FSSP drop spectra (lower right), 2D-C images (upper left), 2D-C spectra (lower left) and text (upper center) are representative of region with rimed ice and aggregates.

Figures 67 and **68** compare the extinction coefficients calculated from FSSP data and SPP-100 data with the extinction coefficient measured on CH6. The FSSP derived values are approximately a factor of 2.5 lower than the CH 6 values. The SPP-100 derived values are approximately a factor of 3 lower than the extinctiometer values. **Figure 69** shows the King LWC (green) and the LWC derived from the FSSP (blue) size distribution and concentration. The FSSP derived values are much lower. **Figure 70** is a scatter plot of the FSSP derived LWC versus the King LWC. The best fit shows the values are reasonably well-correlated (correlation coefficient equal to 0.96), but off by a gain factor of 2.96. The red trace in **Figure 69** is the FSSP LWC with the 2.96 gain factor applied. The result of applying the gain factor is to scale the concentration of particles in each FSSP size bin to make the FSSP derived LWC equivalent to the direct measurement of LWC from the King probe. The FSSP derived extinction coefficient is scaled using this value and plotted in **Figure 71** along with the
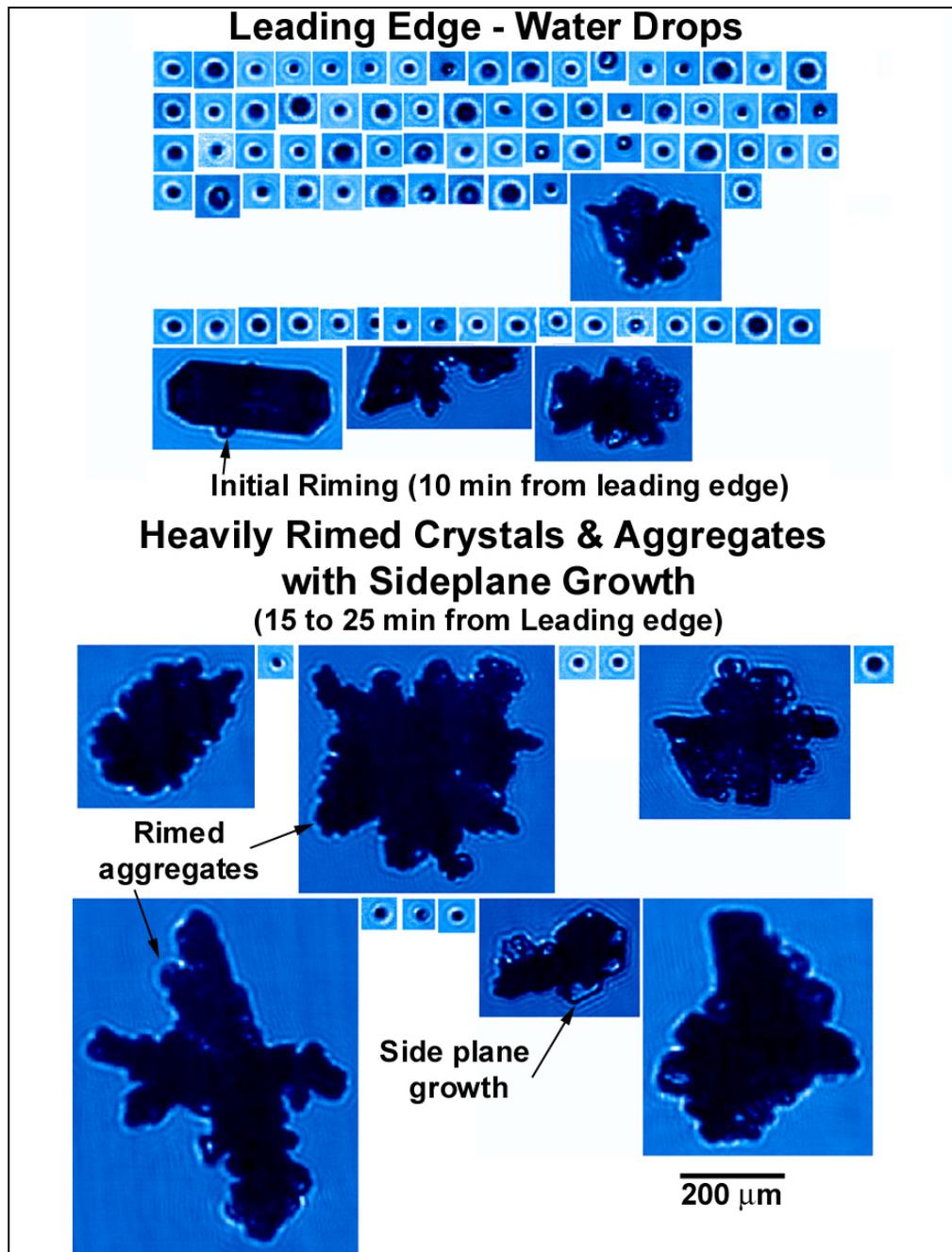
Figure 66. Examples of CPI images of waterdrops and ice particles observed in wave cloud on 26 April 2000.

uncorrected data and the CH6 extinction. **Figure 72** is a scatter plot correlating the corrected FSSP extinction with the CH6 values (correlation coefficient equal to 0.97). The SPP-100 concentration has been scaled to the King LWC using the same procedure. **Figures 73** and **74** show the comparison between the scaled SPP-100 derived extinction and CH6 and the associated scatter plot. The correlation coefficient between the scaled SPP-100 extinction coefficient and the extinctiometer is 0.85.

It should be pointed out that the difference in the FSSP derived extinction on the March 24 flight was 5-6 times lower than the extinctiometer, compared to only 2.5 lower during the April 26 flight. The FSSP was serviced after the April 12 flight, receiving a new laser and new calibration. The principle measurement of the FSSP is drop size, and signals were sorted into 15 equal drop-size bins in the 3-45 μm range. The measurements were summed and recorded every 0.1s. The dynamic accuracy of the FSSP in measuring LWC and drop size is difficult to quantify. Baumgardner (1983) suggests that FSSP measurements of drop size are accurate to 17% and LWC is accurate to within 34%. However, subsequent evaluations of the FSSP have shown additional potential error terms due to coincidences (e.g., Cooper 1988), inhomogeneities in the laser beam and effects of airspeed (e.g., Wendisch et al. 1996). In addition, the accuracy of the FSSP appears to depend on factors that are not always quantifiable, such as field calibrations, optical contamination, airflow effects due to position on the aircraft, etc. Lawson et al (2000) report that FSSP LWC overestimated by a factor of two the adiabatic LWC based on measurements made in adiabatic cloud regions.

Wavelength Dependent Extinction

Figures **68** and **67** are generated using equations (7) and (8) to calculate β_λ for wavelengths corresponding to extinctiometer CH6, CH8, and CH9. The difference in the values of β_λ for the three wavelengths is based on the difference in the extinction cross sections, $\sigma_e(r)$, which depends on the extinction efficiency, Q_{ext}. The SPP-100 generated data shows little to no variation of β_λ with wavelength. The FSSP data shows a slight wavelength dependence between 1850 and 1950 seconds. **Figure 75** is a plot of Q_{ext} for each size bin in the FSSP range at the wavelengths of interest. It can be seen that the largest difference between the wavelengths occurs at only the smallest bin in this FSSP size range, where the 950 nm point has a value of 1.8 and the NIR and IR values are greater than 3.5. At all other size bins, the values of Q_{ext} are within 25% of the values at each wavelength.

Figure 76 shows the FSSP drop spectra at four different times in the cloud. One second averages for drop size distributions are plotted at 1880, 1925, 2012 and 2075 seconds. The mean drop diameter is plotted in **Figure 77**. The plot of mean drop diameter and the size distributions show a mean diameter of about 12.5µm at 1880 and 1925 seconds, decreasing to about 10µm diameter at 2012 and 2075 seconds. Based on the values of Q_{ext} plotted in **Figure 75**, there is not a strong wavelength dependence in the calculated extinction measurements based on the FSSP size spectra. However, qualitatively, the maximum separation occurs between 1850 and 1950 seconds in both the FSSP data and the extinctiometer data, as predicted by Mie theory.

Overall Analysis

Three successful research flights with the airborne extinctiometer demonstrate the airworthiness of the instrument and the ability of the instrument to measure extinction coefficient in a variety of cloud types. **Figure 78** is a scatter plot

showing transmissometer and channel 6 measurements in a combined data set using data from the three successful flights. The correlation coefficient for this plot is 0.93. **Figure 79** is the same as the previous figure with the axis expanded for extinction coefficients below 50 km^{-1}. The scatter in the data improves for each successive flight, suggesting that the modifications to the extinctiometer improved instrument stability.

Korolev et al. (1999) show very good quantitative agreement between the FSSP derived extinction coefficient and measurements made with the Russian Transmissometer during the Canadian Atmospheric Environment Services (AES) Radiation, Aerosol, and Cloud Experiment (RACE) during 1995. **Figure 80** is a plot of extinction coefficient measured with the transmissometer and that derived from FSSP measurements in a warm marine Stratus-Stratocumulus cloud. Korolev et al points out that the good agreement between the derived and measured extinction is due to good tuning of the probes and the absence of droplets outside the FSSP size range, "which in some cases could significantly reduce the calculated values of LWC and extinction".

The mixed phase clouds sampled by the extinctiometer show much more inhomogeneity than the water clouds sampled by Korolev et al. (1999). This can be seen by comparing any of the LWC or extinction values derived from FSSP data with the plots of LWC, extinction and concentration in **Figure 80**. The data collected by SPEC show many peaks and valleys in LWC and drop size over time compared to measurements by Korolev, which were made in warm marine stratus-stratocumulus and vary slowly with time. In addition to the presence of ice, comparison between the FSSP and extinctiometer is further complicated in clouds where spatial properties vary rapidly while flying at aircraft speeds. Also, the 1 Hz data rate of the extinctiometer will have a filtering effect on the extinction measurement, effectively decreasing the magnitude of the fluctuations.

For all three SPEC data flights, the airborne extinctiometer shows good agreement with the tranmissometer during periods of level flight. The FSSP derived extinction is always lower than the measured values. The LWC calculated from the FSSP size spectra and concentration are lower than the LWC measurements with the hot wire probes (about a factor of 3 on April 26 flight). When the FSSP concentration is scaled to provide LWC values consistent with the hot wire probes, the calculated extinction shows good agreement with the measured extinction as plotted in **Figure 71**.

All clouds sampled by the extinctiometer were mixed phase with the 2D-C probe and CPI showing the presence of ice crystals. Typically, the ice was present in much lower concentrations than the water drops, however it is not within the scope of this project to theoretically calculate the effect of ice crystals on the extinction measurement. Future measurements of ice clouds made using the extinctiometer and CPI, to measure particle size, shape and concentration, could be used to validate numerical models of scattering by ice crystals.

2.4.9 Environmental Chamber Test #2

At the conclusion of the flight program, the instrument was taken back to the NCAR environmental chamber to quantitatively evaluate the thermal stability of the new coupling geometry. **Figure 81a** and **b** is a plot of the chamber temperature setpoint and Channel 6 extinction coefficient with the new coupling geometry for the same thermal cycling described previously (**Section 2.4.5**). For temperatures down to –25° C there is significant improvement in the thermal drift compared to the previous test (see **Figure 56b**). The large step changes correlated with the instantaneous change in chamber temperature are no longer present. The maximum drift in the signal for this region is approximately 2 km^{-1}. Below –25° C there is a large spike in the signal, creating a large drift in the baseline measurement. Unfortunately, this step change is more drastic than the maximum change in signal measured during the first environmental chamber test.
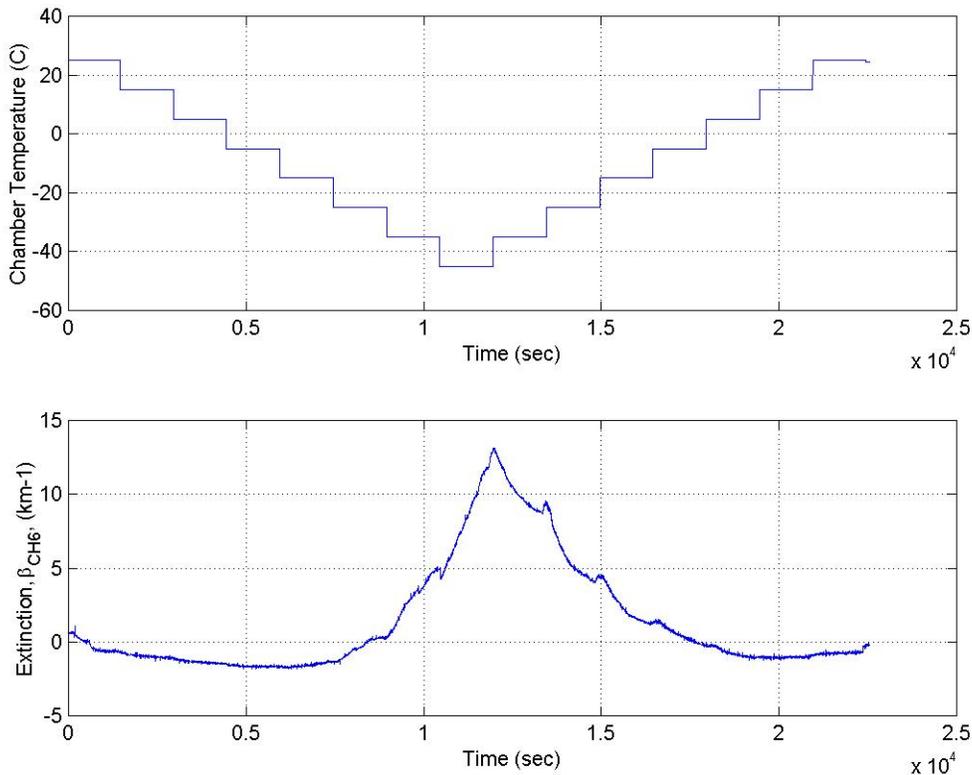

Figure 81. Thermal testing of extinctiometer coupling output beam out far side of Herriott cell. a) chamber temperature and b) CH6 extinction coefficient.

At this time, the cause of this large deviation in the signal at temperatures below –25° C is unknown. It may be possible that the spike is a result of the misalignment of one of the optics modules. The transmitting and receiving optics modules were not realigned at anytime after the initial alignment and it may be

possible that the initial alignment deteriorated over the course of four flights. Further investigation is necessary to determine if the excursion in the signal is caused by a misalignment in one of the components or if the temperature dependent optical stability problem is still present. Due to the short time spent at each temperature set point (25 minutes), it is not clear if the signal is trending toward the baseline value as the thermal mass of the extinctiometer reaches an equilibrium value.

3.0   Recommendations and Commercial Potential

3.1   Recommendations for Future Research

The airborne cloud extinctiometer designed and built in Phase II delivered promising results. The instrument has proven its capability to make reliable airborne measurements of extinction at multiple wavelengths in a variety of cloud types. The data compared well to the Russian tranmissometer, a similar instrument operating at a single waveband and requiring a much longer physical separation between source and detector, and a more elaborate installation on an aircraft. When the FSSP concentration was scaled to the hot-wire LWC value, extinctiometer measurements agreed well with extinction calculated from the FSSP.

Software Control of Filter wheels

Currently, only three wavelengths may be sampled during flight. The position of the filter wheels can be changed manually, between flights, to select a combination of three of the nine wavebands presented in **Table I**. Future work to improve the performance of the instrument includes completing the software control of the filter wheels to allow measurement of all nine spectral channels during flight. By implementing additional DSP code, the filters can be changed while in flight to step through a predefined cycle, or to stay at a particular filter, selectable by the user.

Thermal Stability of Optical Bench

Significant progress was made in evaluating and improving the sensitivity of the extinctiometer, which is limited in flight by thermal stability. Design changes were made to the instrument to improve the stability by coupling the beam out of the far side of the Herriott cell. Further improvements to the thermal stability can be realized by replacing the Amalgon tube used for the optical bench with a material having a lower coefficient of thermal expansion (CTE). Amalgon was chosen for its stiffness, to provide a mechanically stable optical platform. The CTE for Amalgon is approximately the same as that for Aluminum, 13×10^{-6} in./in./$^{\circ}$F. Laboratory and flight testing showed the mechanical rigidity of the optical bench to be satisfactory, the sensitivity of the extinction measurement being limited by thermal changes experienced in flight.

After contacting various manufacturers, a material was found that may prove more thermally stable if used in the optical bench. A carbon fiber tube with the fibers at a 40 degree wrap angle will have a CTE which is approximately 20 times less than the CTE for Amalgon. The stiffness will be about the same as Amalgon, the increased performance being due to the tensile strength of carbon fiber being greater than the tensile strength of E-glass fiber used to fabricate Amalgon. Replacing the tube and testing the instrument in the NCAR environmental chamber would demonstrate the effect of the new material on the thermal stability of the extinction measurement.

Spectral Stability of QTH Source

Currently, CH6 has the highest sensitivity with the least amount of drift in the signal. This is because the reference detector uses the identical filter as CH6. Any power fluctuations of the light source in this waveband are effectively normalized out of the measurement. Based on laboratory and flight testing, the other channels drift more than CH6 as a function of QTH lamp temperature. This is because while controlling the output of the lamp to a constant power in a specific waveband, the spectral output of the lamp shifts at other wavelengths as a function of drive voltage and ambient temperature. By controlling the ambient temperature around the lamp, the spectral stability can be improved. This can be accomplished by installing a heater and sensor on the lamp housing and using it to maintain the housing at a constant temperature.

Future Flights in Other Cloud Types

Future research flights in other cloud types will provide a richer data set for extinctiometer performance characterization and inter-comparison of instruments. Flying in homogeneous, all water clouds will provide a better data set for comparing the FSSP calculated extinction with the measured extinction. The ability of the extinctiometer to detect wavelength dependence of the extinction coefficient can be verified by flying in clouds having a narrow size spectra with a modal diameter that shifts between 8 and 11µm, where the extinction efficiency, Q_{ext}, exhibits significant differences in two of the channels.

Flights in cirrus clouds would demonstrate the ability of the extinctiometer to consistently measure very low values of extinction coefficient, below $5 - 10$ km^{-1}. The fiber mount in the optical bench of the instrument failed during the only cirrus flight of this project. Flights in cirrus would determine if the extinctiometer has low enough sensitivity in the current configuration or if the design changes proposed above would need to be implemented to make the measurements. Measurements in cirrus may be of the highest scientific interest of all cloud types.

Application of Numerical Modeling Results to Collected Data

Numerical modeling has been performed to characterize the response of the extinctiometer to different drop sizes at different wavelengths. For most types of clouds encountered, the model predicts the measured value will be within 30% of

the theoretical value at all wavelengths. Given a size distribution from the FSSP, it would be possible to correct the extinctiometer measurements to exclude the forward-scattered light collected due to the Herriott cell.

3.2   Commercial Potential

The cloud extinctiometer would be useful to collect data for in situ validation of remote sensing instruments. The Aqua (EOS PM-1) satellite will launch in December 2000 carrying the MODIS FM-1 instrument. MODIS uses a variety of spectral channels to look at properties of the atmosphere, ocean and land masses. The extinctiometer uses two of the same spectral channels used by MODIS to look at cloud properties.

The First International Satellite Cloud Climatology Program (ISCCP) Regional Experiment (FIRE) Cirrus Regional Study of Tropical Anvils and Cirrus Layers (CRYSTAL) is a comprehensive scientific program consisting of modeling and observational programs and integrated analyses designed to address the important questions surrounding tropical cirrus cloud systems and their roles in both regional and global climates. FIRE.CRYSTAL will consist of two experimental phases. The first phase, Florida Area Cirrus Experiment (CRYSTAL-FACE), will occur in 2002 and the second phase, Tropical Western Pacific (CRYSTAL-TWP), will occur in 2004. In situ aircraft measurements and observations from the Aqua satellite are of primary importance to the FIRE.CRYSTAL program. Measurements from the extinctiometer would be valuable in understanding the radiative properties of the types of cirrus clouds to be studied in these experiments. SPEC is planning to pursue funding to fly the extinctiometer on at least one of the aircraft platforms in the FIRE.CRYSTAL field programs.

In addition to FIRE.CRYSTAL, SPEC will collect additional data with the extinctiometer on the SPEC Learjet. We anticipate publishing a paper to stimulate interest in extinctiometer measurements within the scientific community. By making the scientific community aware of the capabilities of the extinctiometer, some commercial instrument sales may be realized.

Water Turbidity and Dust Laden Environment Measurements

A proof of concept laboratory experiment was performed to demonstrate the application of the measurement technique used in the extinctiometer for measurements of water turbidity. Water turbidity is an indicator of cloudiness in water due to suspended solids. A cylindrical measurement cell was constructed from transparent acrylic. The ends of the cell were optically clear and the dimensions were selected to allow insertion of the cell into the beam path within the optical bench. It was necessary to increase the gain on the detector preamplifier to compensate for the attenuation of the acrylic windows. The signal decreased substantially because the beam intercepts the windows fifty times while traversing 25 passes through the cell. (This was the reason for avoiding protective windows in the airborne extinctiometer design.)

Figure 82. Measurements of water turbidity were made by inserting a water-filled, clear acrylic cell into the extinctiometer optical path.

The cell was filled with water and an unknown concentration of glass beads ranging from 5 to 60 microns in diameter was mixed into the cell. The cell was vigorously shaken to stir up the beads and then inserted into the optical path. **Figure 82** is a photograph of the cell inserted into the optical bench. **Figure 83** is a plot of the extinction coefficient due to scattering and absorption of the glass beads in the cell. As time progresses, the beads begin to settle out and a baseline signal is reached. To minimize the attenuation of the beam in water, the measurements were made using Channel 2, operating at 550 nm. The maximum extinction coefficient measured, approximately 550 km^{-1}, was much higher than the values encountered in clouds.

Measurements of water turbidity are usually made in units of Jackson Turbidity Units (JTU) or Nephelometric Turbidity Units (NTU). JTUs are measured by turbidity instruments that measure light attenuation in the forward direction, while NTUs are measured by looking at the ratio of forward attenuated light to light scattered at 90 degrees (a detector looking at 90 degrees is also needed). There is not a straightforward conversion of extinction coefficient to JTUs or NTUs, primarily because the index of refraction and shape of particles found in water can vary greatly. Instead, a formazin solution calibration standard is used. The formazin standard has very stable scattering properties (given in NTU) and is used to calibrate turbidity instruments.
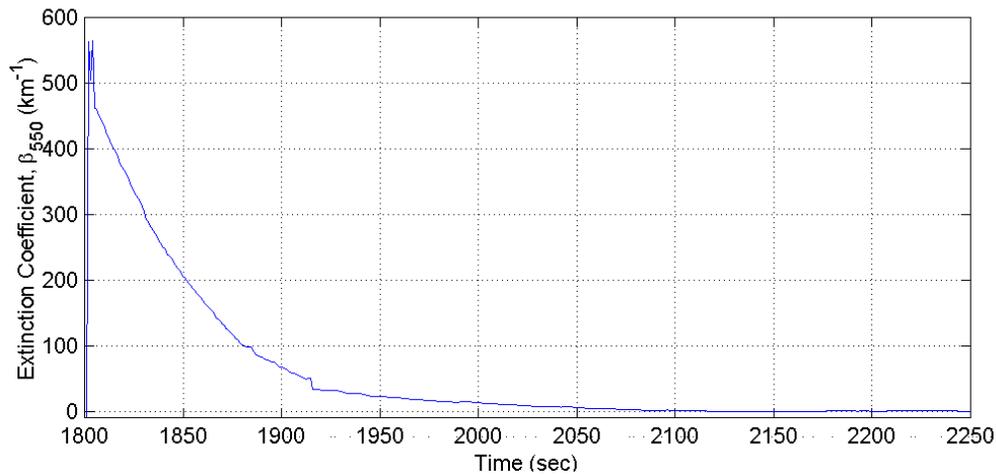
Figure 83. Extinction measurement of glass beads in water. The plot shows the beads eventually settle out and a baseline signal is reached.

The measurement technique used in the extinctiometer, as well as the electrical and optical design methodologies, can be implemented in the design of a turbidity meter. The optical pathlength can be chosen depending on the levels of turbidity to be measured. For instance, the Environmental Protection Agency (EPA) has established regulatory guidelines for the acceptable limits for drinking water at 0.3 NTU. The levels for industrial wastewater would be much higher (100 –1000 NTU). A variety of design configurations could be realized, from measuring turbidity in a closed cell as done in the laboratory, to lowering only the optical bench and fibers into a body of water to make turbidity measurements at different depths.

Measurements of extinction in dust-laden environments can be performed with the existing instrument. Depending on the maximum values, the optical path could be shortened to prevent the signal from saturating. As in the case of water turbidity measurements, the instrument can be repackaged for different types of environments. A variety of configurations are achievable, from measuring dust in grain silos to measuring opacity in power plant emissions.

4.0 References

Ardanuy, P. E., and H. L. Kyle, 1986: El Niño and outgoing longwave radiation: Observations from Nimbus 7, ERB, *Mon. Weather Rev.*, **114**, 415-433.

Arking, A., 1991: The radiative effects of clouds and their impact on climate. *Bull. Am. Meteor. Soc.* **72**, 795-813.

Baumgardner, D., 1983: An analysis and comparison of five water droplet measuring instruments, *J. Appl. Meteor.*, **22,** 891-910.

Baumgardner, D., and A. Rodi, 1989: Laboratory and wind tunnel evaluation of the Rosemount Icing Detector. *J. Atmos. Oceanic Technol.,* **6,** 971-979.

Cooper, W. A., 1988:Effects of coincidence on measurements with a forward scattering spectrometer probe, *J. Oceanic Atmos. Tech.,* **5**, 823-832.

Herriott, D., Kogelnik, H., and Kompfner, R., 1964: Off-Axis Paths in Spherical Mirror Interferometers, Applied Optics, Vol. **3** No. 4, 523-526.

House, F. B., 1965: The radiation balance of the earth from a satellite, Ph.D. thesis, p. 69, Univ. of Wis.

Irvine, W.M. and J.B. Pollack, 1968: Infrared optical properties of water and ice spheres, *Icarus*, **8**, 324-360.

King, W. D., D. A. Parkin and R. J. Handsworth, 1978: A hot wire liquid water device having fully calculable response characteristics, *J. Appl. Meteor.,* **17**, 1809-1813.

Knollenberg, R.G. : 1981, Techniques for probing cloud microstructure, in Clouds, their formation, Optical Properties, and Effects.

Korolev, A.V., J.W. Strapp, G.A. Isaac and A.N. Nevzorov, 1998: The Nevzorov Airborne Hot wire LWC-TWC Probe: Principle of operation and performance characteristics, *J. Atmos. Oceanic Technol.*, **15**, 6,1495-1510.

Korolev, A.V., Isaac, G.A., and Strapp, W.J., 1999: In situ measurements of effective diameter and effective droplet number concentration, *J. Geophys. Res.*, **104**, D4, 3993-4003.

Lawson, R. P. and A. M. Blyth, 1998: A comparison of optical measurements of liquid water content and drop size distribution in adiabatic regions of Florida cumuli. *Atmos. Res.*, **47-48**, 671-690.

Lawson, R.P., B.A. Baker and C.G. Schmitt, 2000: Overview of microphysical properties of summertime boundary layer clouds observed during FIRE.ACE. Submitted to *J. Geophys. Res.* Special Issue on FIRE.ACE (to download this paper go to the following website and, under the JGR Special Issue header,

scroll down to the paper and click on it:
http://paos.colorado.edu/faculty/curry_home/GEWEX/publications

Liou, K.N., 1980: An Introduction to Atmospheric Radiation, Academic Press.

May, R.D., 1998: Open-path Near-Infrared Tunable Diode Laser Spectrometer for Atmospheric Measurements of H2O, accepted for publication in *Jour. of Geophys. Res*.

Nevzorov, A.N., and Shugaev, V.F., 1974: Aircraft cloud extinction meter (in Russian), *Trans. Of Cent. Aerol. Obs.,* **106**, p 3-10.

Particle Measuring Systems, 1977: Operator's Manual for Forward Scattering Spectrometer Probe.

Pilewskie, P. and F. P. J. Valero, 1995: Direct observations of excess solar absorption by clouds. *Science*, **267** 1626-1629.

Stephens, G. L. and S-C Tsay, 1990: On the cloud absorption anomaly, *Q. J. R. Meteorol. Soc.,* **116**, 671-704.

Trutna, W. R., and Byer, R.L., 1980: Multi-pass Raman gain cell, Applied Optics, Vol **19** No. 2 p301-312, January.

Valero, F. P. J., T. P. Ackerman, W. J. Y. Gore, 1983: Radiative effects of the Arctic haze. *Geophys. Res. Lett.*, **10**, 1184.

Vonder Haar, T. H., and V. E. Suomi, 1969: Satellite observations of the earth's radiation budget, *Science,* **163**, 667-667.

Vonder Haar, T. H., and V. E. Suomi, 1971: Measurements of the earth's radiation budget from satellites during a five-year period, extended time and space means, *J. Atmos. Sci.,* **28**, 305-314.

Webster, C.R., May, R.D., Trimble, C.A., Chave, R.G., and Kendall, J., 1994: Aircraft (ER-2) laser infrared absorption spectrometer (ALIAS) for in situ stratospheric measurements of HCL, N_2O, CH_4, NO_2, and HNO_3, Applied Optics, **33**, 454-472.

Wendisch, M., A. Keil, and A.V. Korolev, 1996: FSSP characterization with monodisperse water droplets, *J. Atmos. Oceanic Technol.*, **13**, *6*, 1152-1165.